Computational Materials Science 253 (2025) 113844

Contents lists available at ScienceDirect

Computational Materials Science

journal homepage: www.elsevier.com/locate/commatsci

Full length article

Introducing long-range particle interactions into phase-field models of sintering using continuum mechanics principles

Vladimir Ivannikov [a,*], Peter Munch [b], Thomas Ebel [a], Regine Willumeit–Römer [a], Christian J. Cyron [a,c]

[a] Helmholtz-Zentrum Hereon, Max–Planck-Straße 1, Geesthacht, 21502, Germany
[b] Technical University of Berlin, Straße des 17. Juni 136, Berlin, 10623, Germany
[c] Technical University of Hamburg, Eißendorfer Straße 42, Hamburg, 21073, Germany

ARTICLE INFO

Dataset link: https://github.com/hpsint/hpsint

Keywords:
Solid-state sintering
Phase-field methods
Coupled modeling
Finite element method
Materials modeling
Microstructure evolution

ABSTRACT

This work presents a novel meso-scale phase-field model of solid-state sintering that couples the continuum thermodynamics and continuum mechanics governing the sintering process. The microstructure evolution is described by a system of equations consisting of one Cahn–Hilliard equation and a set of Allen–Cahn equations to distinguish neighboring particles. These equations are coupled with the balance of momentum of linear elasticity. The latter is defined by applying the Wang sintering forces as distributed body loads to compute advection velocities for the phase-field equations. This introduces long-range interaction mechanisms between particles. Our numerical implementation uses monolithic coupling and implicit time integration. It is based on the `hpsint` code, an efficient matrix-free finite element solver for phase-field simulations of many-particle sintering processes with advanced grain tracking capabilities and block preconditioning. With a simple academic test setup that analyzes a chain of identical particles we investigate in detail the problems of the original sintering model proposed by Wang around two decades ago and then clearly demonstrate how our new coupled approach resolves them. We then study a series of two- and three-dimensional benchmark problems to demonstrate the advantages of our novel model that clearly exhibits invariance of shrinkage regarding the model size (number of particles in the packing) and renders microstructures whose metrics agree well with estimates based on analytical and experimental studies.

1. Introduction

Solid-state sintering has been studied by scientists for decades but only became widely used by manufacturers when advanced and robust binder-assisted shaping techniques, such as metal injection molding [1] and 3D printing [2], enabled the reproducible production of green parts with complex shapes and sufficient density. With these technologies now available, the industry's focus has shifted towards optimizing sintering process parameters to ensure desirable microstructures, shrinkage control, and optimal mechanical properties. These features strongly depend on the powder characteristics and sintering conditions, including atmosphere, maximum temperature, hold time at the maximum temperature, additional holding steps, and heating and cooling rates. Optimizing the entire sintering time–temperature profile remains a key challenge and is currently performed mainly by trial and error, which is expensive, time-consuming, and suboptimal, as it is nearly impossible to test all combinations of manufacturing parameters. Therefore, there is a pressing need to complement and partially replace experiments with predictive computer simulations.

To resolve both microstructure and shrinkage[1] evolution, meso-scale models, i.e., models at the scale of individual particles, are typically required. Application scenarios include, for instance, the manufacturing of patient-specific biodegradable magnesium implants [3], where the mechanical properties and the biodegradation process significantly depend on both the geometry and microstructure of the

* Corresponding author.
E-mail addresses: vladimir.ivannikov@hereon.de (V. Ivannikov), muench@math.tu-berlin.de (P. Munch), thomas.ebel@hereon.de (T. Ebel), regine.willumeit@hereon.de (R. Willumeit–Römer), christian.cyron@hereon.de (C.J. Cyron).

[1] One should keep in mind the subtle difference between the terms "shrinkage" and "densification". The former refers to the geometric changes of a part during sintering, whereas the latter primarily describes the increase in the relative density of a part, which also encompasses corresponding microstructural changes (i.e., pore elimination). However, since these two terms are closely related (shrinkage is hardly possible without underlying microstructural changes and vice versa), we use them interchangeably throughout the text.

https://doi.org/10.1016/j.commatsci.2025.113844
Received 6 January 2025; Received in revised form 13 March 2025; Accepted 14 March 2025
Available online 10 April 2025

implant [4]. Various numerical techniques are available for studying sintering at the meso-scale, but not all are capable of handling both aforementioned quantities of interest. For instance, Monte–Carlo simulations [5] capture mainly grain evolution, whereas the mechanisms responsible for shrinkage are often introduced in rather artificial, heuristic manners and often render unphysical behavior like inhomogeneous densification [6,7] that needs a further special treatment [8]. The discrete element method (DEM) can address both microstructure evolution and shrinkage [9–11], but its ability to capture grain coarsening during the later stages of sintering, despite recent advances [12], remains questionable due to the underlying geometric assumptions regarding particle shapes.

Phase-field approaches can resolve both grain evolution and shrinkage at a feasible computational cost. In particular, the recent progress in high-performance computing (HPC) has led to the rapid emergence of powerful generalized phase-field simulation frameworks and specialized tools for modeling sintering, such as `PACE3D` [13,14], `Tusas` [15], `OpenPhase` [16,17], `PRISMS-PF` [18], and `MOOSE` [19–21].

Most phase-field models of sintering are based on the landmark work of Wang [22] and use the Cahn–Hilliard and Allen–Cahn equations to describe microstructure evolution. Wang's model introduced the concept of sintering forces to capture the rigid-body motions of particles and, thus, shrinkage, albeit with certain limitations. The behavior of this model has been extensively studied and advanced in the subsequent works. For example, the Wang formulation was enhanced in [23] by incorporating tensorial mobility instead of the originally considered scalar one, improving the description of mass fluxes on the surface and at the grain boundaries. It was demonstrated in [24] how real material data can be integrated into numerical simulations. The effects of grain orientation and anisotropic grain boundary properties were discussed in detail in [25].

A significant amount of effort has been devoted to identifying the nuances in the evaluation of sintering forces and improving the advection mechanisms introduced by Wang. For instance, the studies reported in [21] were based on the implementation of the Wang model in `MOOSE`[19], a modern modular finite element method (FEM) framework. This code, among other useful features, includes a grain tracking algorithm [26] that allows multiple grains to be mapped to a single order parameter. This functionality has optimized and simplified the evaluation of sintering forces for multiparticle systems. A similar order parameter reassignment strategy, but in the context of a finite difference (FD) implementation, was used in [27], where the effect of the Wang densifying forces was demonstrated for systems containing several hundred particles. The computation of the advection velocities used in [21] was also simplified by eliminating interpolation over the order parameters. Another notable simplification was proposed in [28], where the rotational effects were omitted, allowing two prefactors k and m_t to be merged into one. While a 2-particle system was studied in [21], a 3-particle system was used in [29] to investigate the influence of rigid-body motions on pore shrinkage.

From its inception, the concept of sintering forces as introduced by Wang [22] lacked a rigorous theoretical foundation and was based primarily on heuristic assumptions. This led to multiple revisions of the definition of sintering forces. Initially, Wang's sintering forces required the evaluation of integrals over each inter-particle contact zone. This operation significantly increases computational cost and introduces non-local terms in FEM discretizations, which are difficult to linearize when an implicit time-stepping scheme is used. To address this issue, [30] computed the forces based solely on the deviation of the phase-field variables at a single point — specifically, at the center of the inter-particle contact zone. Another alternative formulation for computing the advection velocities was proposed in [31]. This approach is based on the free energy change due to particle motion, which should minimize in equilibrium. The idea was successfully validated through a series of 2D two-particle simulations, with the results compared to existing experimental data, proving to be a reasonable alternative to the original definition from [22].

The rigid-body motions during sintering were thoroughly benchmarked in [32] using a specifically designed test involving a linear chain of identical particles. In a subsequent contribution [33], the authors demonstrated how the Wang advection mechanism can be integrated into a different, grand-potential phase-field model originally derived in [14]. This latter work also showed the incorporation of CALPHAD databases [34] into the model to describe the energy properties of real materials and, moreover, was the first to report large-scale phase-field sintering simulations of systems containing thousands of particles. In addition to adopting the Wang forces for a grand-potential sintering model, several improvements were proposed in [33] for evaluating the equilibrium concentration value at the grain boundary, which deviates from that in the bulk due to local geometric effects. The work also clearly revealed a significant limitation of Wang's advection formulation: the dependence of the obtained shrinkage on packing size. To resolve this issue, the same authors proposed in [35] to use molecular dynamics simulations to study the influence of atomic mass transport during pore elimination on the size of the simulated domain for a simple geometry. These observations were then translated to a phase-field model as advective rules of motion. While promising and capable of delivering invariance of shrinkage regarding system size, this concept introduced a predefined behavior derived from a numerical model of a different type, which brings certain drawbacks (such as heuristic assumptions and, specifically due to the use of molecular dynamics, a high computational cost). Nevertheless, [33] represents a significant advancement compared to the original [22] and most commonly used phase-field approaches in handling particle advection.

In addition to this large family of works, where the advection behavior was ultimately defined using the idea of Wang [22], there are several contributions proposing original and distinctly different approaches for incorporating rigid-body motions into numerical analyses using the phase-field technique. One such approach coupled the phase-field and discrete element methods [36]. This work employed background DEM simulations, where surface tension forces were used to compute particle advection fields, which were then incorporated back into the phase-field equations. However, this approach has not been further developed due to its high complexity and the questionable applicability of surface tension forces in the context of solid-state (as opposed to liquid-phase) sintering. In [37], the authors derived a grand-potential phase-field model in which the rigid-body motions of particles were formulated around the hypothesis that vacancies arrive at a grain boundary and remain there until a complete vacancy layer is formed. When a grain boundary between two particles has a continuous layer of vacancies, the two particles move toward each other as rigid bodies. Thus, under this hypothesis, the rigid-body motions driving shrinkage are controlled by the grain boundary vacancy diffusion rate and the modified equilibrium concentration of vacancies at grain boundaries (segregation). While this is an interesting idea, it remains unclear to what extent it can realistically capture the shrinkage of large particle packings, as the derived phase-field equations do not explicitly include advection components.

The popularity of Wang's advection formulation and the underlying sintering force terms stems from their simplicity and the ability to incorporate shrinkage mechanisms into practically any phase-field sintering model with relatively low effort. However, as demonstrated later in the present work, there are certain fundamental drawbacks to Wang's sintering forces that inherently lead to physically unrealistic behavior.

In the current work, we analyze these aspects and propose an alternative approach to incorporating densification behavior into phase-field models of sintering. To this end, the phase-field equations are coupled with continuum mechanics, allowing the advection velocities to be derived from the solution of a coupled elasticity problem. This

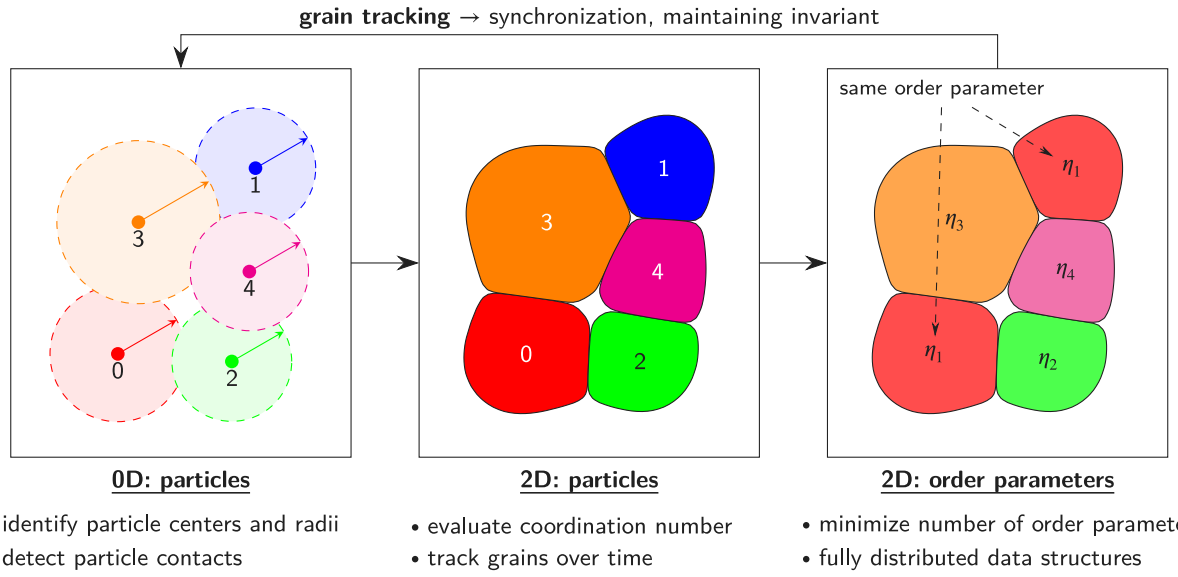

Fig. 1. The particle representations available in `hpsint` and the key information each provides relevant to the present work. The representations are illustrated for a sample case of a 5-particle packing in 2D. We maintain a 0D representation of particles described by their position, radius, and additional statistical quantities. This reduced model is used for postprocessing, to determine potential contacts between grains, and to ensure that order parameters can only include non-neighboring particles, which may involve remapping certain grains within the solution vectors.
Source: Adopted from [38].

problem is defined by replacing Wang's sintering forces with statically equivalent distributed body forces for each particle. In this way, we can address one of the most significant issues of Wang's original formulation of the sintering forces: its inability to capture long-range interactions between particles.

Our new model is implemented in our matrix-free phase-field code `hpsint` [38], which is available on GitHub.[2] As its backbone, the code utilizes the open-source library `deal.II` [39–41].

The work is structured as follows. In Section 2, we recall the original phase-field formulation of Wang [22], along with its advection terms, which are critically discussed in Section 3, where we study sintering using the simple academic example of a chain of identical circular particles in two dimensions. This section explains why the chain's shrinkage unphysically decreases as the number of particles in the chain increases when using Wang's sintering forces. In Section 4, we present our new model, which couples a thermodynamic phase-field model with a linear elasticity problem. Section 5 discusses numerical examples, and finally, Section 6 summarizes our conclusions.

In this work, first- and second-order tensors are printed in italic boldface, fourth-order tensors in capital double-struck, and discretized quantities in boldface. Scalar and cross products are denoted as $\cdot$ and $\times$, respectively, while double contraction products of two second-order tensors are indicated by a colon.

2. Wang's phase-field sintering model

2.1. Governing equations

We recall the phase-field model of solid-state sintering introduced in [22], which is based on a system of Cahn–Hilliard and Allen–Cahn equations:

$$\frac{\partial c}{\partial t}(\boldsymbol{x},t) = \nabla\cdot\left[M\nabla\frac{\delta F}{\delta c}\right] - \nabla\cdot(\boldsymbol{v}c)\,, \tag{1a}$$

$$\frac{\partial \eta_i}{\partial t}(\boldsymbol{x},t) = -L\frac{\delta F}{\delta \eta_i} - \nabla\cdot\left(\boldsymbol{v}_i\eta_i\right). \tag{1b}$$

[2] https://github.com/hpsint/hpsint

where t denotes time, $\boldsymbol{x}$ is the position vector in space $\mathcal{R}^d$, and N is the number of particles in the packing. As usual, $\nabla\cdot\boldsymbol{p} = \operatorname{div}\boldsymbol{p}$ is the divergence of an arbitrary tensor $\boldsymbol{p}$ with the spatial derivatives being gathered in a vector operator $\nabla = \left(\frac{\partial}{\partial x_1},\ldots,\frac{\partial}{\partial x_d}\right)$. The set of variables η_i describes individual particles (or grains; in this work, we use these terms interchangeably): $\eta_i = 1$ inside the ith particle and $\eta_i = 0$ elsewhere. The variable c represents the molar fraction of the material, i.e., *concentration*; therefore, $c = 1$ inside any of the particles and $c = 0$ in the voids. For optimization purposes, it is common to reuse [26,42,43] the same variable η_i for multiple non-interacting particles. The variable η_i is then referred to as an *order parameter* and groups multiple particles together. We have previously [38] developed an efficient, fully distributed algorithm for constructing such groups in an optimal manner, thus minimizing the number of order parameters in use. This algorithm employs the grain tracking feature that synchronizes the spatial and reduced 0D representations of individual particles, and, depending on the microstructure topology, remaps them between the domain unknowns when needed, see Fig. 1.

The kinetics of the system containing N particles is determined by the free energy

$$F = \int_\Omega \left[f\left(c,\eta_i\right) + \frac{1}{2}\kappa_c|\nabla c|^2 + \sum_i^N \frac{1}{2}\kappa_\eta|\nabla\eta_i|^2 \right] \mathrm{d}\Omega, \tag{2}$$

where

$$f\left(c,\eta_i\right) = Ac^2(1-c)^2 + B\left[c^2 + 6(1-c)\sum_i^N \eta_i^2 - 4(2-c)\sum_i^N \eta_i^3 + 3\left(\sum_i^N \eta_i^2\right)^2\right] \tag{3}$$

is the chemical free energy density contributing to the bulk and interface energies, and the remaining two gradient terms provide additional contribution to the interface energy. The energy parameters A, B, κ_c, and κ_η can be derived from the surface and grain boundary energy values of the material, as shown in [24].

The mass transport is captured by the Cahn–Hilliard equation and is introduced through various diffusion mechanisms described by the

mobility term [22]:

$$M = M_{\mathrm{vo}}\phi + M_{\mathrm{va}}(1-\phi) + 4M_s c^2(1-c)^2 + M_{\mathrm{gb}}\sum_{i=1}^{N}\sum_{j\neq i}^{N}\eta_i\eta_j, \tag{4}$$

where $\phi = c^3\left(10 - 15c + 6c^2\right)$. Here, the subscripts "vo", "va", "s", and "gb" denote the mobility coefficients for the volumetric, vapor, surface, and grain boundary paths, respectively. For simplicity, the scalar form (4) of the mobility is used in this work. Alternatively, one can introduce the so-called tensorial mobility, as proposed in [23]. Implementation details of this approach in the context of high-performance matrix-free methods are provided in [38]. Similar to M, the parameter L from the Allen–Cahn equations defines the mobility of grain boundaries and thus describes the intensity of grain coarsening. Both M and L can be expressed via the Arrhenius formula by defining the corresponding prefactors and activation energies [21], to account for the increase in mobility with rising sintering temperature.

2.2. Introducing rigid-body motions

The conventional Cahn–Hilliard and Allen–Cahn equations directly address the mass-transport-related aspects of sintering. However, shrinkage mechanisms induced by the compressive stresses arising in the vicinity of grain boundaries due to the rapid diffusion of atoms remain completely missing. These processes may evoke complex particle interactions in large, realistic packings, resulting in significant microstructure changes. To resolve this issue, Wang [22] added to system (1) the corresponding advection terms, where $\boldsymbol{v} = \sum_i^N \boldsymbol{v}_i$ and the advection velocity within individual particles $\boldsymbol{v}_i$ consists of translational and rotational components:

$$\boldsymbol{v}_i(\boldsymbol{x}) = \begin{cases} \boldsymbol{v}_{t\,i}(\boldsymbol{x}) + \boldsymbol{v}_{r\,i}(\boldsymbol{x}), & \text{if inside a particle} \\ 0, & \text{otherwise} \end{cases} \tag{5}$$

with

$$\boldsymbol{v}_{t\,i}(\boldsymbol{x}) = \frac{m_t}{V_i}\boldsymbol{F}_i, \tag{6a}$$

$$\boldsymbol{v}_{r\,i}(\boldsymbol{x}) = \frac{m_r}{V_i}\boldsymbol{T}_i \times \left(\boldsymbol{x} - \boldsymbol{x}_{c\,i}\right), \tag{6b}$$

where m_t and m_r are coefficients characterizing the magnitude of the particle translation and rotation velocities with respect to the sintering force and where

$$V_i = \int_\Omega \eta_i \,\mathrm{d}\Omega \tag{7}$$

is the particle volume. The vector $\boldsymbol{x}_{c\,i}$ denotes the mass center of the ith particle. The velocity components $\boldsymbol{v}_{t\,i}$ and $\boldsymbol{v}_{r\,i}$ are proportional to the force and torque [22], respectively, given by

$$\boldsymbol{F}_i = \int_\Omega \mathrm{d}\boldsymbol{F}_i, \tag{8a}$$

$$\boldsymbol{T}_i = \int_\Omega \left(\boldsymbol{x} - \boldsymbol{x}_{c\,i}\right) \times \mathrm{d}\boldsymbol{F}_i. \tag{8b}$$

The effective local force density $\mathrm{d}\boldsymbol{F}_i$ is the key component of the entire shrinkage mechanism and is computed as

$$\mathrm{d}\boldsymbol{F}_i = k\sum_{j\neq i}\left(c - c_0\right)\zeta\left(\eta_i\eta_j\right)\left[\nabla\eta_i - \nabla\eta_j\right]\mathrm{d}\Omega. \tag{9}$$

Here, c_0 is the equilibrium value of the mass concentration at the grain boundary, meaning the force vanishes when $c = c_0$. The factor k is a *sintering force coefficient* that describes the dependency of the sintering forces on the mass concentration imbalance at the grain boundaries. The term $\zeta\left(\eta_i\eta_j\right)$ acts as a filter identifying grain boundaries through the order parameters:

$$\zeta\left(\eta_i\eta_j\right) = \zeta\left(\eta_i\eta_j\right)_{\mathrm{Wang}} = \begin{cases} 1, & \text{if } \eta_i\eta_j \geq s_{gb}, \\ 0, & \text{otherwise}, \end{cases} \tag{10}$$

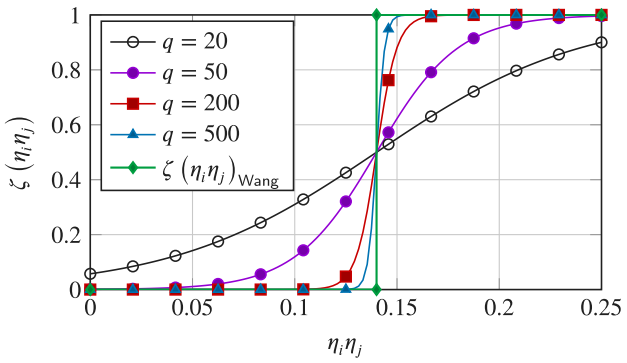

Fig. 2. Visualization of the continuous grain boundary filter function $\zeta\left(\eta_i\eta_j\right)$ for different values of the smoothening parameter q, threshold value $s_{gb} = 0.14$.

where s_{gb} is the threshold value, which we usually set to 0.14 following the practices of the other researchers [27,32]. However, in [32], it was observed that this discontinuous definition of $\zeta\left(\eta_i\eta_j\right)$ leads to jumps in the advection velocities. In our case, since we use an implicit time marching scheme, this term may result in poor convergence of Newton iterations. To eliminate this discontinuity, we redefine $\zeta\left(\eta_i\eta_j\right)$ as

$$\zeta\left(\eta_i\eta_j\right) = \frac{1}{1 + e^{-q\left(\eta_i\eta_j - s_{gb}\right)}} \tag{11}$$

Fig. 2 shows how this continuous function behaves within the range of $\eta_i\eta_j \in [0\ldots0.25]$ for different values of q. The upper limit of the range is determined by the fact that at each point in the domain, $\sum_i^N \eta_i = 1$, and therefore, for a grain boundary between two arbitrary particles described by order parameters η_i and η_j, $\max\left(\eta_i\eta_j\right) = 0.25$ when $\eta_i = \eta_j = 0.5$. The minimum value of q is then constrained by the requirement that $\zeta(0) \to 0$ and $\zeta(0.25) \to 1$. For this reason, the curve for $q = 20$ in Fig. 2 clearly violates this restriction. Our numerical experiments revealed that one should choose $q \geq 50$. A detailed analysis of the influence of this parameter on the accuracy of the numerical results is presented in Supplementary Material S1, from which the only important outcome we need to refer at the moment is that all numerical simulations from Section 5 are performed using (11) with $q = 200$.

3. Critical analysis of Wang's phase-field model

3.1. The advection terms

As pointed out in the introduction, the approach proposed by Wang [22] has been widely and successfully used by many researchers for both small- and large-scale simulations. To capture shrinkage, Wang introduced elementary compressive forces per unit area at the grain boundary (9), computed from the difference between the effective mass concentration and its corresponding equilibrium value. The advection velocities are then defined to be proportional to this quantity, as seen in expressions (6), (8), and (9). The idea is clear and reasonable: the higher the imbalance of mass concentration at the grain boundary, the larger the forces, and the more intensive the densification. This behavior correlates well with what is observed in practice: indeed, the shrinkage rate is higher in the early stages of sintering when the necks are yet relatively small and actively growing. Moreover, its numerical implementation is relatively simple while effectively capturing the desirable effects, at least qualitatively.

However, one should recall that this concept is not based on any rigorous theoretical derivations and was rather intuitively constructed. The lack of a sound theoretical foundation is, in itself, not an overly serious issue for the model. What makes it crucial is the fact that certain components of the introduced heuristics may significantly limit the practical applicability of the Wang approach. In particular, the explicit

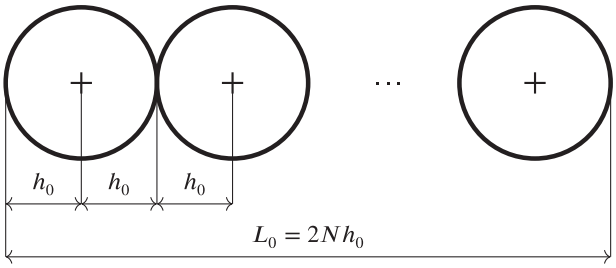

(a) Initial configuration.

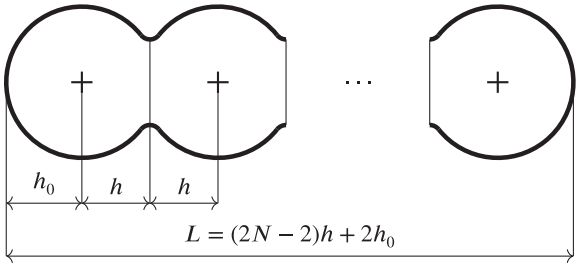

(b) Final configuration.

Fig. 3. Sintering of a chain containing N identical particles.

linear dependency (6) between forces and velocities — an assumption that notably simplifies computations — may easily lead to non-physical behavior, especially pronounced in some edge cases.

3.2. Benchmark: a chain of identical particles

To illustrate the aforementioned issues, consider a chain containing N identical particles, all having a radius r_0 at the time instance t_0, as shown in Fig. 3. For the given material, fixed sintering conditions, and identical green density values, the real metallic parts having different dimensions exhibit identical shrinkage. This observation should also apply to the chain geometry from Fig. 3, and therefore one should expect shrinkage along the horizontal axis to be independent of N provided $N \to \infty$. Indeed, let $h_0 = r_0$ be the distance between a particle's center and one of its grain boundaries at t_0. After sintering, this distance reduces to $h < h_0$. The initial and final lengths of the chain are then given as

$$L_0 = 2Nh_0 \quad \text{and} \quad L = (2N-2)h + 2h_0, \tag{12}$$

respectively. The shrinkage of the chain can then be computed as follows:

$$\varepsilon = \frac{L_0 - L}{L_0} = \frac{N-1}{N}\left(1 - \frac{h}{h_0}\right). \tag{13}$$

The shrinkage invariance is then evident since

$$\varepsilon \to \left(1 - \frac{h}{h_0}\right) \text{ if } N \to \infty. \tag{14}$$

Expression (13) implies that the outside semicircles of two particles on the ends of the chain retain the same shape as in the initial configuration, so that the distance from their center to the outside edge of the particle remains h_0. This is a reasonable assumption given that the chemical potential in those outmost regions is constant along the particle surface due to the constant curvature of the latter. A detailed justification of this assumption is presented in Supplementary Material S2.

Let us now analyze the behavior of the chain based on the definition of sintering forces (9). For such geometry, at the initial time instance t_0, forces $\boldsymbol{F}_i = 0\ \forall i \neq \{1, N\}$ due to symmetry, since the grain boundary effects for each particle in the interior cancel each other. Only $F_1 \neq 0$ and $F_N \neq 0$, and therefore, at t_0, particles 1 and N start moving towards their neighbors. If the advection velocities are low, then the additional mass brought to the neck area does not influence the grain boundary fluxes, and the growth rates remain identical for all the necks in the chain. Consequently, all forces $\forall i \neq \{1, N\}$ remain zero throughout the entire process, with only the outermost particles exhibiting rigid-body motions and contributing to shrinkage.

However, if the advection velocities are sufficiently high to alter the mass fluxes along the grain boundaries between particles $1, N$ and their direct neighbors $i = 2$ and $i = N-1$, then forces $\boldsymbol{F}_2$ and $\boldsymbol{F}_{N-1}$ are no longer zero. This delayed process, in which the particles gradually push their neighbors, propagates along the entire chain, resulting in all forces $\boldsymbol{F}_i$ ultimately becoming different from zero. The exact magnitudes and even signs of these forces depend on the interplay of the grain boundary diffusion and advection properties, specifically M_{gb}, m_t, and k (with m_r being irrelevant in this geometry). Thus, all particles in the chain exhibit rigid-body motions, contributing to shrinkage; however, it remains unclear whether the resulting shrinkage is homogeneous and how it aligns with the estimate (14).

To investigate these two questions in more detail and to verify this preliminary analysis, we implemented the original formulation (1) and ran simulations for chains of different lengths with $N = \{2, 4, 6, 8, 10, 12\}$ measuring the shrinkage of this system along the x-axis. Only even values of N are considered to simplify the subsequent analysis of strains in the chain, however, any packing with an odd number of particles exhibits qualitatively the same behavior. The initial radius of the particles was set to $r_0 = 10$, and the material energy properties were defined as $A = 17.4$, $B = 0.6$, $\kappa_c = 2.25$, and $\kappa_\eta = 0.5$. The diffusion prefactors were set to $M_{\text{vo}} = 0.01$, $M_{\text{va}} = 10^{-10}$, $M_{\text{s}} = 4$, and $M_{\text{gb}} = 0.4$, while the grain boundary mobility was defined as $L = 1$. The advection properties were chosen as $m_r = 0$, $m_t = 1$, with k varied in the range $30 \ldots 3000$. By selecting these advection-related parameters, we effectively eliminate m_r and m_t from discussion and focus solely on the magnitude of k. This approach simplifies further comparisons with the later-presented coupled model, which does not employ (6) and, therefore, contains neither m_r nor m_t. According to the analytical limit studies from [24], the chosen energy parameters render the diffuse interface having thickness $w \approx 1.0$. For numerical analysis, we used the matrix-free FEM-based implementation of the model in our code `hpsint`, which was previously thoroughly validated in [38]. Only the 2D case was analyzed, as the chain shows no qualitative differences in its behavior in 3D.

Numerical studies were performed for three different values of the sintering force coefficient k: 30, 300, and 3000. As seen in Fig. 4(a), as expected, the low value $k = 30$ does not induce significant advection velocities capable to initiate the densification process of the entire chain, resulting in only the outermost particles contributing to the shrinkage behavior. In this scenario, the length of the chain after sintering is merely given by

$$L = (2N-2)h_0 + 2h, \tag{15}$$

and its shrinkage can therefore be estimated as

$$\varepsilon = \frac{L_0 - L}{L_0} = \frac{1}{N}\left(1 - \frac{h}{h_0}\right), \tag{16}$$

from which $\varepsilon \to 0$ if $N \to \infty$. However, if the prefactor k is increased to $k = 300$ or $k = 3000$, the outermost particles start influencing their neighbors, emitting more complex particle interactions and leading to more pronounced shrinkage, as seen in Figs. 4(b) and 4(c). Though large values of the sintering force coefficient k lead to greater shrinkage and involve more than just the outermost particles in the densification process, they still do not meet the analytical estimate (13). Furthermore, the curves in Figs. 4(b) and 4(c) show that although the shrinkage for $N > 2$ is larger than for $N = 2$, the strain ε still

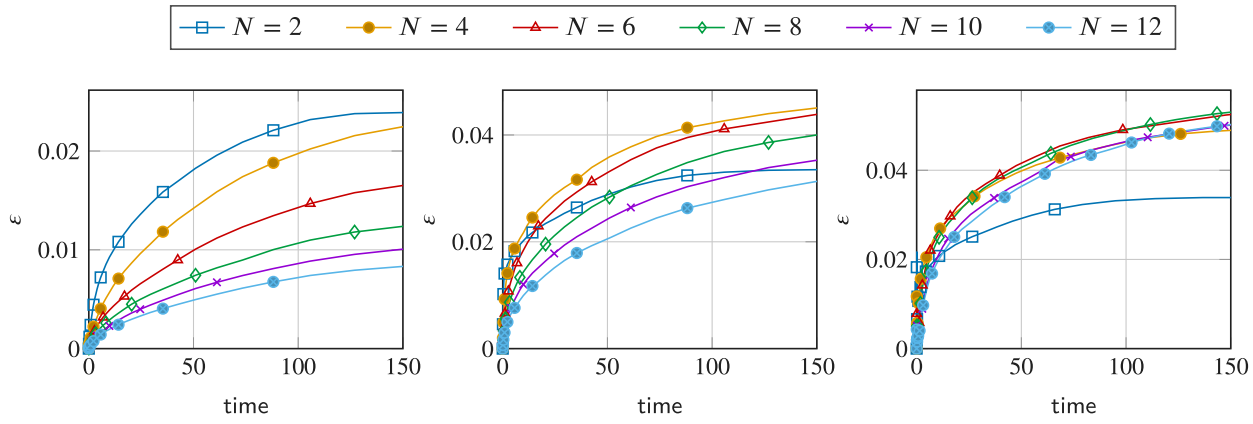

(a) $k = 30$. (b) $k = 300$. (c) $k = 3000$.

Fig. 4. Shrinkage of the particle chain with different numbers of particles N and sintering force coefficient k, using the original Wang model with a grain boundary diffusion prefactor $M_{\text{gb}} = 0.4$.

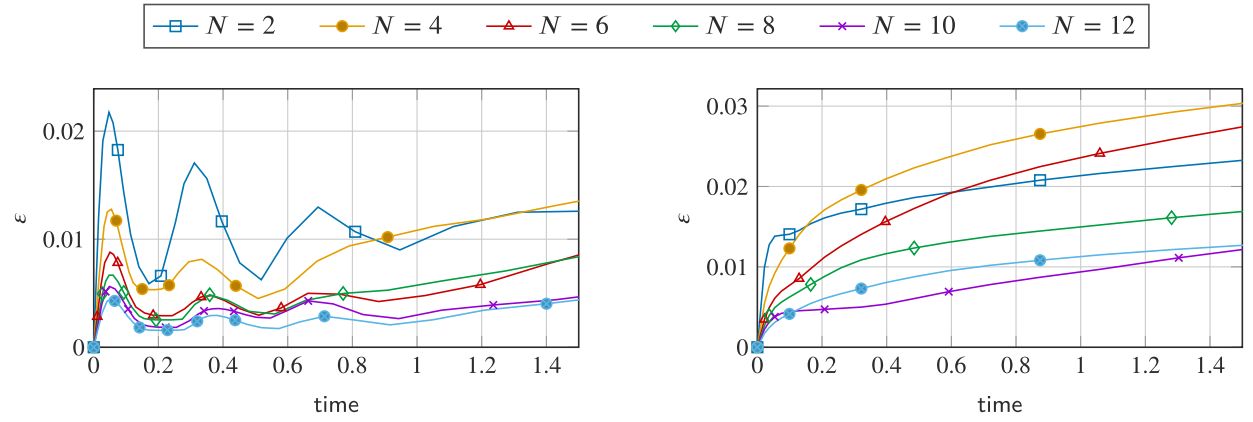

(a) grain boundary diffusion prefactor $M_{\text{gb}} = 0.4$.. (b) grain boundary diffusion prefactor $M_{\text{gb}} = 4$..

Fig. 5. Unphysical shrinkage oscillations of the particle chain at the initial phase of the simulation for different N and a sintering force coefficient $k = 3000$ when using the original Wang model.

decreases as N increases. Overall, the curves presented in Figs. 4(b) and 4(c) initially seem to confirm the observation from [29] that suggests beyond a certain threshold, further increases in k have little effect on shrinkage. However, a more detailed analysis of shrinkage-related quantities (strains within this section and velocities in Supplementary Material S3.1) for different grain boundary diffusion parameters reveals that this statement is not entirely correct.

Another unphysical defect that can be observed when the original Wang sintering forces are used is the mechanical oscillations. They are introduced by the wave-like propagation of the advection behavior along the chain axis and get reflected in the shrinkage curves, especially for large values of k. They are not visible in Fig. 4(c) due to the x-axis scale, but their presence becomes apparent when zoomed in, as shown in Fig. 5(a). These oscillations are inevitable and are a side effect of the shrinkage mechanism introduced by (6) and (9).

The observed oscillations indicate that the advection fluxes supply excessive amounts of mass to the neck region, such that it cannot be timely transported then by the grain boundary diffusion mechanism from the neck center to its surface. The increase of the grain boundary diffusion prefactor M_{gb} indeed alleviates this issue. As seen in Fig. 5(b), the oscillations are no longer present in the sintering curves, but they are still inconsistent for different N and far from being in agreement with the estimates provided by (13), see Supplementary Material S3.1 for more details.

A perfectly homogeneous strain field is expected during sintering for the chain geometry due to its symmetry. To verify this, we compute the axial strain measure $\widetilde{\varepsilon}_{ij}$ between the centers of two symmetrically opposite particles, i and j, in the chain:

$$\widetilde{\varepsilon}_{ij} = \frac{(x_{j\,0} - x_{i\,0}) - (x_j - x_i)}{(x_{j\,0} - x_{i\,0})}. \tag{17}$$

Since the particles are always selected symmetrically, we note that $j = N - i$ and simplify the notation by dropping the second index in $\widetilde{\varepsilon}_{ij}$, referring to this quantity simply as $\widetilde{\varepsilon}_i$, where the subscript then represents the pair number. Although the grain tracker feature of `hpsint` provides the center coordinates of individual particles, we cannot use this information to accurately evaluate (17) because the locations of the particle centers of mass change not only due to advection but also due to the geometric evolution of the particles themselves (e.g., neck growth). To eliminate this additional dependency, at each time instance t_k, numerically integrated with timestep τ_k, we compute the position of the ith particle center of mass from its previous value and the current advection velocity as follows:

$$x_{i\,k} = x_{i\,k-1} + v_{xi\,k-1}\tau_k. \tag{18}$$

Fig. 6 illustrates the evolution of $\widetilde{\varepsilon}$ for six pairs of particles in a 12-particle chain at three different values of the sintering force coefficient k. The curves clearly indicate that the strain field generated by the

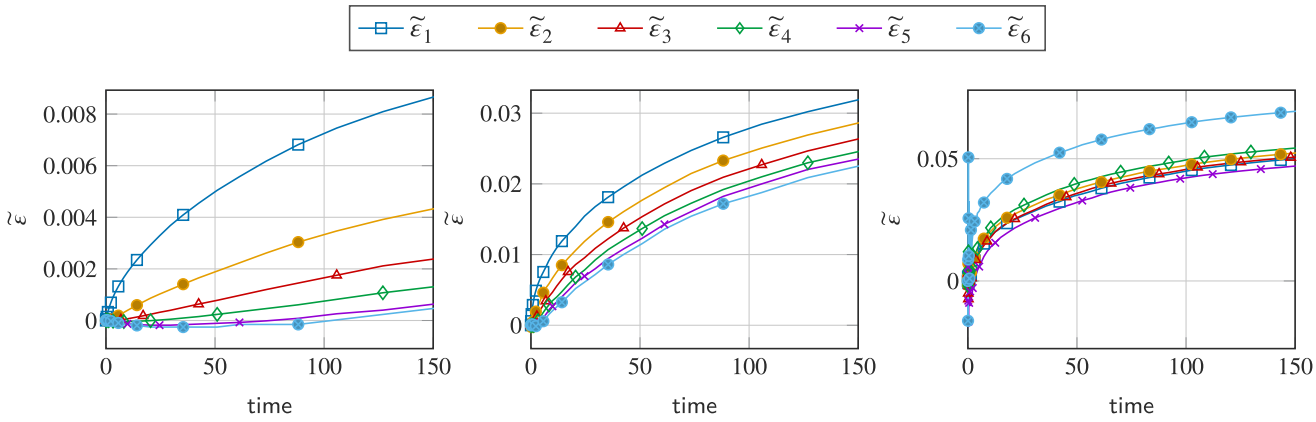

(a) $k = 30$. (b) $k = 300$. (c) $k = 3000$.

Fig. 6. Shrinkage strain $\widetilde{\varepsilon}_i$ computed for 6 pairs of symmetrically located particles in a chain with $N = 12$, for different sintering force coefficient k, using the original Wang model with a grain boundary diffusion prefactor $M_{gb} = 0.4$.

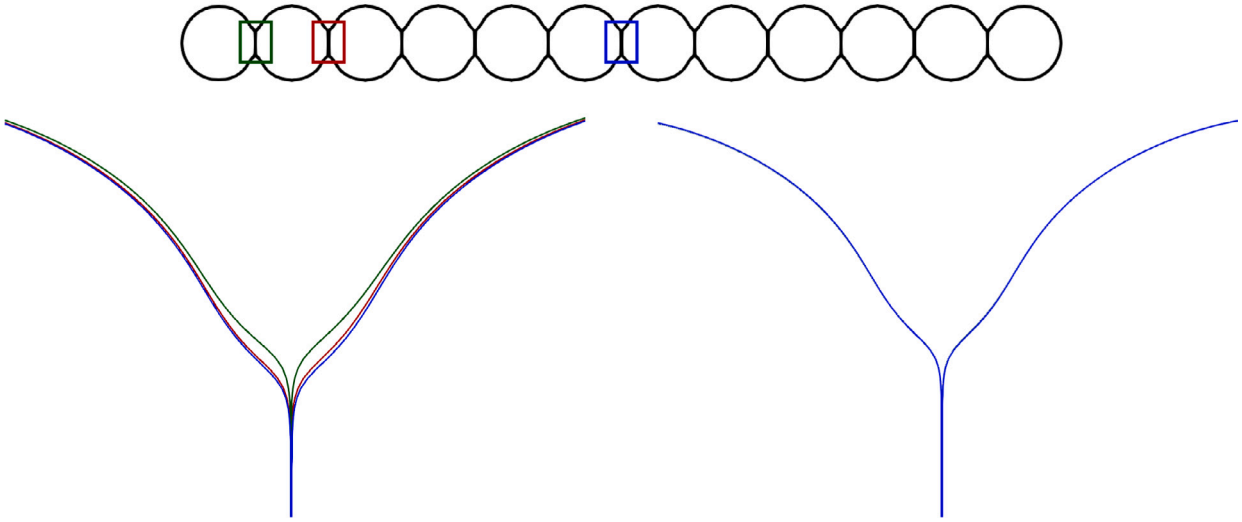

(a) Original Wang model, $k = 300$. (b) Coupled model, $k = 0.1$.

Fig. 7. Comparison of the necks formed between the different pairs of particles of the 12-particle chain at time instance $t = 2.25$ using the original Wang and the proposed coupled models, grain boundary diffusion prefactor $M_{gb} = 0.4$.

original Wang model is not homogeneous; however, the results improve significantly for larger values of k. These observations align perfectly with those in Fig. 4.

On the microstructure level, inhomogeneous shrinkage gets reflected also in forming such necks within a symmetric chain which are different from each other. As seen in Fig. 7(a) that compares the necks for three different contact pairs of the 12-particle chain, the very left neck is larger than the others whereas the central one reveals to be the smallest. This is again related to the wave-like propagation of advective behavior across the packing that initiates from the outmost particles of the packing.

A very similar inconsistent densifying behavior was reported in [32], where a chain of N particles with slightly different geometry and material properties was analyzed. Although the problem of the Wang formulation was not explicitly addressed in that work, Figure 4(b) from [32], especially if rescaled using a linear scale instead of logarithmic, exhibits a steady decrease in shrinkage as the number of particles in the chain increases.

This unphysical behavior of the Wang model is particularly evident in this simple edge case benchmark. In more practically relevant tests, when the initial packing is formed as a scattered assembly of randomly distributed particles with different radii, this side effect is less visible but still present. For instance, Termuhlen et al. [27] performed an in-depth analysis of rigid-body effects in large three-dimensional packings containing hundreds or thousands of particles. In Figure 7(d) of [27], they show the contour lines on the $z = 10$ μm plane taken at the end of the sintering process, highlighting the difference between the cases when advection was accounted for and when it was not. It is possible to observe that the outer contours indeed exhibit rigid-body motions toward the center of the entire sintered structure, but this effect is significantly less pronounced in the packing interior. This is due to the fact that the forces are more prone to compensate each other in the bulk rather than on the packing surface.

Another manifestation of this problem can be observed in the results obtained by Seiz et al. in [33], where the sintering of three different cubic packings containing 263, 3446, and 34460 particles was simulated. Figure 6 from [33] shows a clear dependency of shrinkage on the scale of the packings: the largest packing exhibits significantly lower densification.

From the analyzed chain benchmark and the other numerical examples shown in the literature, we can summarize the following limitations of the original Wang advection formulation:

1. the proposed shrinkage mechanism lacks a physically grounded and rigorous foundation,
2. it may introduce unphysical oscillations in the packing, and the appearance of these oscillations is difficult to predict,
3. it may lead to significantly different densification behavior for similar systems, even when they differ only slightly in scale,
4. the obtained densification is not homogeneous even for packings with evenly distributed particles, and
5. shrinkage decreases with an increase in system size.

The source of all these problems stems from the artificial nature of the force–velocity linear dependency (6) and the heuristic definition of sintering forces (9).

4. Novel coupled phase-field sintering model

4.1. Coupling phase-field model with continuum mechanics

In order to resolve the limitations described in Section 3, we must recall that sintering is, in fact, a multiphysics process that couples mass transport and mechanical phenomena. In the late 1960s, Johnson [44], through rigorous physics-based derivations, demonstrated the role of the stresses induced at the grain boundary by the evolution of chemical potential due to material flow as a driving force for sintering, particularly shrinkage. He then successfully applied the constructed equations to obtain volume, grain boundary, and surface diffusion coefficients from experimental sintering data.

Keeping this important concept in mind, we introduce the conventional continuum mechanics static equilibrium

$$\nabla \cdot \boldsymbol{\sigma} + \boldsymbol{b} = 0, \tag{19}$$

which needs to be solved at each timestep in addition to the original phase-field equations. Here $\boldsymbol{\sigma}$ and $\boldsymbol{b}$ represent the domain stresses and distributed body forces, respectively. The latter are composed of individual forces uniformly distributed over the volume V_i of the corresponding particle, as given by

$$\boldsymbol{b} = \sum_i \eta_i \frac{\boldsymbol{F}_i}{V_i}. \tag{20}$$

Similarly, as in [22], the forces $\boldsymbol{F}_i$ are computed using expressions (9) and (8a).

One must choose a suitable constitutive relation for the mechanical part of the model. Since the sintering process occurs at high temperatures close to the material's melting point, viscoelastic material behavior should generally be considered. However, even for simple viscoelastic models (e.g., the Maxwell model), the numerical implementation of the discrete FEM solution scheme based on Eqs. (19) and with (1) coupled together proves to be exceptionally challenging for the following reasons:

1. stresses and strains need to be accumulated over time for viscoelastic materials,
2. phase-field equations are constructed using the Eulerian specification, whereas the mechanical ones usually operate on the Lagrangian frame of reference [45].

These aspects necessitate a complex time history tracking procedure, along with a technique to appropriately transfer relevant quantities of interest between the Lagrangian and Eulerian grids, such as through the use of an arbitrary Lagrangian–Eulerian approach [46,47]. For the initial benchmarking and verification of the proposed coupling concept, we deemed this strategy excessive. To avoid these complications, we introduce another hypothesis at this point.

We assume that the material viscosity is sufficiently small compared to the timescale of the sintering process (as well as the individual timesteps in our simulations), allowing us to consider that a fully relaxed state is achieved at each timestep. This assumption is fundamental to the currently derived coupled model and implies that the mechanical stress generated during the sintering process is relaxed infinitely fast. This hypothesis is reasonable for the behavior of metals at elevated temperatures over timescales of several hours. Consequently, a much simpler, linear elastic material constitutive relation can be employed:

$$\boldsymbol{\sigma} = \mathbb{D}_{\text{eff}} : \boldsymbol{\varepsilon}_e \tag{21}$$

with

$$\mathbb{D}_{\text{eff}} = c\mathbb{D}, \tag{22}$$

where the concentration c is also used to account for the presence of voids in some parts of the domain, and $\mathbb{D}$ is the elasticity tensor of the solid phase.

Since metallic parts do not typically exhibit large deflections during sintering and densification is driven by meso-scale processes, small strain elasticity can be considered. Therefore, the displacements translate into the strain field via

$$\boldsymbol{\varepsilon} = \frac{1}{2}\left(\frac{\partial \boldsymbol{u}}{\partial \boldsymbol{x}} + \frac{\partial \boldsymbol{u}}{\partial \boldsymbol{x}}^T\right). \tag{23}$$

The assumption regarding the infinitely fast relaxation of the arising mechanical stress also allows one to interpret the displacement field $\boldsymbol{u}$ obtained from the solution of (19) as particle advection velocities

$$\boldsymbol{v} = \boldsymbol{u} \quad \text{and} \quad \boldsymbol{v}_i = \boldsymbol{u}, \tag{24}$$

which are then plugged into the phase-field system (1). This is a very important result that, together with (20), completes the coupling between the mass transport and mechanical phenomena in the proposed model. Note that, distinctly from the original Wang formulation, the velocity $\boldsymbol{v}$ entering the Cahn–Hilliard equation (1a) is no longer a sum of individual $\boldsymbol{v}_i$.

The coupled model derived herein introduces more complex interaction mechanisms between powder particles during sintering: the velocity is obtained now from the displacements of the mechanical model. This can be understood as a version of the Wang model where particles are no longer conceptualized as largely separate mechanical entities but as parts of a mechanical continuum, so that long-range interactions between distant particles due to elastic coupling through intermediate particles are now (unlike in the Wang model) automatically accounted for.

The proposed model, though, is still not fully physically consistent since the body forces (11) are computed at the moment using the original heuristics proposed by Wang [22]. However, each force $\boldsymbol{F}_i$, still being applied locally over the ith particle only, now has an influence on the entire packing, distinctly from the situation when relations (6) are used.

4.2. Weak form and preconditioning

The system (1) and Eq. (19) are solved at each timestep in a monolithically coupled manner. After introducing the chemical potential $\mu = \delta F/\delta c$ as an auxiliary variable, expanding explicitly the variational derivatives $\delta F/\delta c$ and $\delta F/\delta \eta_i$, and exploiting the definition (2), the complete system of equations can be written as

$$\frac{\partial c}{\partial t} = \nabla \cdot [M \nabla \mu] - \nabla \cdot (\boldsymbol{v} c), \tag{25a}$$

$$\mu = \frac{\partial f}{\partial c} - \kappa_c \nabla^2 c, \tag{25b}$$

$$\frac{\partial \eta_i}{\partial t} = -L\left[\frac{\partial f}{\partial \eta_i} - \kappa_p \nabla^2 \eta_i\right] - \nabla \cdot (\boldsymbol{v}_i \eta_i), \tag{25c}$$

$$\nabla \cdot (\mathbb{D}_{\text{eff}} : \boldsymbol{\varepsilon}) + \boldsymbol{b} = 0. \tag{25d}$$

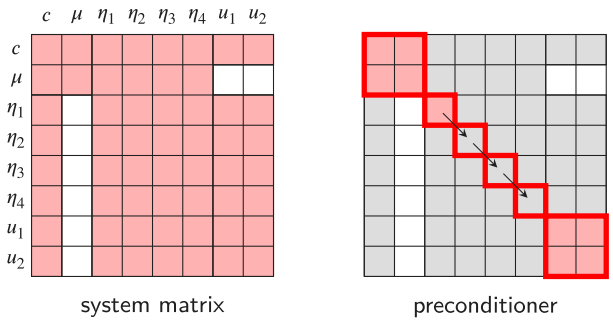

Fig. 8. Visualization of the block sparsity pattern of (1) the system matrix and of (2) the considered preconditioner obtained when discretizing (26) for the case of four order parameters and a 2D displacement field.

By denoting the test functions for an arbitrary variable β as φ_β, the weak form of system (25) then reads as

$$\left(\varphi_c,\ \frac{\partial c}{\partial t}\right) = -\left(\nabla\varphi_c,\ M\nabla\mu\right) - \left(\varphi_c,\ \nabla c\cdot\boldsymbol{v}\right) - \left(\varphi_c,\ c\,\nabla\cdot\boldsymbol{v}\right), \tag{26a}$$

$$\left(\varphi_\mu,\ \mu\right) = \left(\varphi_\mu,\ \frac{\partial f}{\partial c}\right) + \left(\nabla\varphi_\mu,\ \kappa_c\nabla c\right), \tag{26b}$$

$$\left(\varphi_{\eta_i},\ \frac{\partial \eta_i}{\partial t}\right) = -\left(\varphi_{\eta_i},\ L\frac{\partial f}{\partial \eta_i}\right) - \left(\nabla\varphi_{\eta_i},\ L\kappa_p\nabla\eta_i\right) - \left(\varphi_{\eta_i},\ \nabla\eta_i\cdot\boldsymbol{v}_i\right) - \left(\varphi_{\eta_i},\ \eta_i\nabla\cdot\boldsymbol{v}_i\right), \tag{26c}$$

$$\left(\nabla\varphi_{\boldsymbol{u}},\ \mathbb{D}_{\text{eff}} : \boldsymbol{\varepsilon}\right) - \left(\varphi_{\boldsymbol{u}},\ \boldsymbol{b}\right) = 0. \tag{26d}$$

The boundary integrals emerging from integration by parts vanish since zero natural boundary conditions are considered for all phase-field components. Note also that, distinctly from the situation where we used velocities (5), the divergence terms $\nabla\cdot\boldsymbol{v}$ and $\nabla\cdot\boldsymbol{v}_i$ do not vanish, since the advection components are computed using (24), and the displacement field $\boldsymbol{u}$ is an arbitrary continuous function. The first three equations of (26) are scalar, whereas the last one is written for a vectorial unknown $\boldsymbol{u}$. The weak form (26) then results in a nonlinear system $\mathbf{R}(\mathbf{d}) = 0$, with all the unknowns gathered in the vector $\mathbf{d} = \begin{bmatrix} c & \mu & \eta_i & \boldsymbol{u}\end{bmatrix}^T$. The implicit BDF2 scheme is applied, and `NOX` from the `Trilinos` library [48] is used as a nonlinear solver, as was done in [38]. The reader is referred to this work for the details regarding the linearization of $\mathbf{R}(\mathbf{d})$.

The sparsity pattern of the Jacobian matrix corresponding to the FEM discretization of the weak form (26) is illustrated in Fig. 8. Its high complexity arises from the definitions of free energy (2), mobility (4) and body forces (20). Since `hpsint` is a matrix-free code, only iterative linear solvers can be utilized, necessitating the selection of an appropriate preconditioner. The topic of preconditioning of the phase-field part of the coupled model is discussed in detail in [38], where we proposed a specifically constructed block Jacobi preconditioner that employs incomplete LU (ILU) factorization for the Cahn–Hilliard equation and blockwise averaged ILU for the Allen–Cahn ones. Now, we need to add a third component to the preconditioner to address the mechanical part of the model. To this end, we employ algebraic multigrid (AMG) [49], setting the polynomial degree of the Chebyshev smoother to 6 and applying 7 multigrid cycles.

4.3. Stiffness matrix ill-conditioning

By examining (21) and (22), one can easily identify a potential numerical issue for the discretized problem: void regions deliver zero contributions to the resultant tangent matrix, rendering it singular. To resolve this issue, we limit the minimum material stiffness within the domain by replacing (22) with

$$\mathbb{D}_{\text{eff}} = \min(c, 0.1)\,\mathbb{D}. \tag{27}$$

This approach is straightforward to implement and, and preliminary numerical tests indicate that a minimum value of $c_{\min} = 0.1$ has no significant impact on the results. Without this strategy, we would need to address the cells with zero stiffness by eliminating the corresponding degrees of freedom from the finite element assembly. This would require frequent reconstruction of the underlying sparsity pattern at each timestep, which is a costly operation in our case.

4.4. Dirichlet boundary conditions

To solve the linear elastic problem, Dirichlet boundary conditions are required, and their imposition is not straightforward in the present case. Since we generate computational domains such that the packings are always surrounded by void padding [38], applying constraints at the boundaries is not physically relevant, especially when elastic properties are defined as in (27). To circumvent this issue, we impose zero displacement constraints over specific cell faces within the computational domain according to the following algorithm.

First, the *mass center* O of the packing is identified, as illustrated in Fig. 9. Using the simplified 0D particle representation, shown in Fig. 1, we then determine the *reference point* R as the centroid C_m of a *growing* grain m nearest to O:

$$R = C_m\ :\ \|\boldsymbol{x}_{C_m} - \boldsymbol{x}_O\| \to \min\ \wedge\ V_{mk} > V_{mk-1}, \tag{28}$$

where V_m is the grain volume as computed by (7). Condition $V_{mk} > V_{mk-1}$ implies that the mth grain has grown between the two consecutive time instances t_k and t_{k-1}. This guards the algorithm against selecting a grain that might be the closest but is on the verge of being consumed by neighboring grains due to grain growth. Our experience shows that choosing a very small particle can result in too few mechanical constraints being enforced on the packing, significantly degrading the convergence of both linear and nonlinear iterative solvers. The application of condition (28) is illustrated in Fig. 9, where the centroid of particle 3 is chosen as the reference point, while particle 4, though an eligible candidate, is discarded.

In the next step, the active cell containing the reference point R is identified within the mth particle. The coarsest parent of this active cell is then tracked, and the vertex closest to R is selected as the *origin point* Q with coordinates $\boldsymbol{x}_Q$. For the d-dimensional space, the individual components u_j of the displacement vector $\boldsymbol{u}$ are restrained over d hyperplanes passing through vertex Q. These constraints are applied not over the entire hyperplanes but only to points within particle m, which was previously detected using condition (28). If particle m is mapped to an order parameter η_i, then the resulting mechanical constraints applied to the packing can be written as

$$u_j = 0\ \forall\ x_j = x_{jQ}\ \wedge\ \eta_i(\boldsymbol{x}) \geq \eta_{\text{lim}}. \tag{29}$$

Condition (29) is a heuristic engineering approach, designed for easy implementation to benchmark the coupling between the phase-field and mechanical models. However, one should be aware of its side effects. The presented strategy for imposing essential boundary conditions violates certain principles of continuum mechanics, particularly equilibrium in the vicinity of the restrained region, since the constraints are applied in the domain's interior rather than on its boundary. To mitigate the extent of equilibrium violation, we introduced the second condition in (29). Naturally, a more rigorous method for applying these constraints should be developed, but this is deferred for future work.

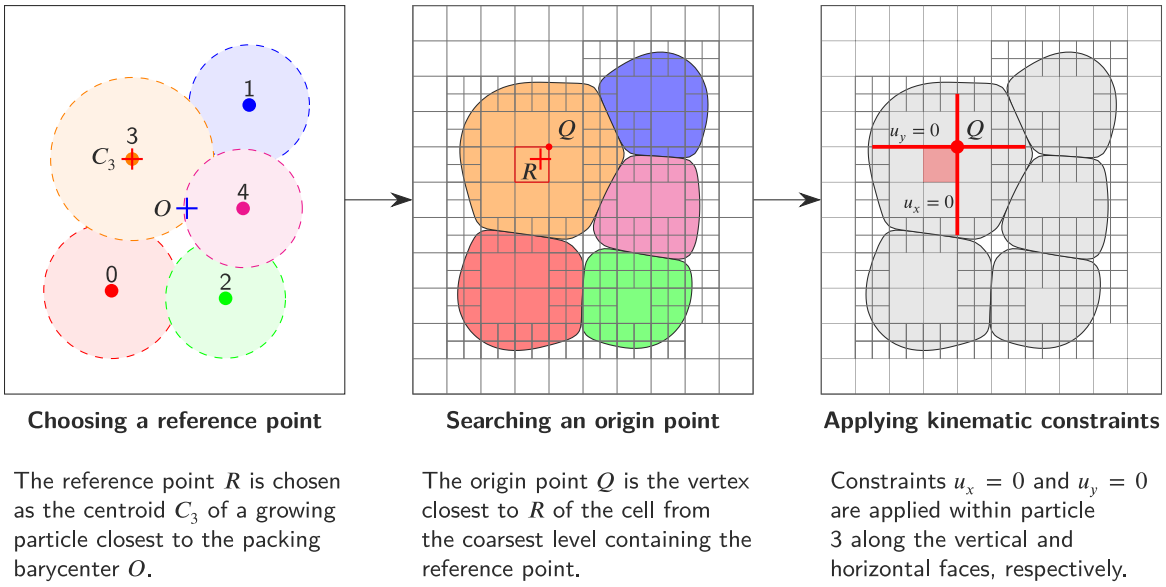

Fig. 9. Imposing kinematic boundary conditions for different choices of the reference point for the case of sintering of 5 particles in 2D with adaptive mesh refinement.

4.5. Defining the model parameters

In addition to the parameters related to the phase-field part of the model and introduced in Section 3, the conventional elastic mechanical properties, such as the Young's modulus E and Poisson's ratio ν, also need to be specified. It is important to remember that the mechanical part of the formulation, in its current form, lacks a direct physical counterpart. While it effectively captures the mechanism, it currently has no solid theoretical foundation. Consequently, the mechanical properties can be set somewhat arbitrarily, aimed at simplifying the overall calibration process. Typically, we assign $E = 1$ and $\nu = 0.25$.

The intensity of the shrinkage forces is then governed solely by the coefficient k, unlike in the original Wang model, where $m_r = 0$ and $m_t = 1$ are used for ease of comparison with the coupled formulation, as stated in Section 3. Since the forces $\boldsymbol{F}_i$ are utilized differently in each of the models — acting as mere velocities in the original Wang model via (6) and as distributed body loads via (20) in the coupled model — the parameter k will differ significantly in value and even in orders of magnitude between the two. To ensure comparative simulations, once k is identified for the Wang model, it is then adjusted for the coupled model so that the same shrinkage behavior over time is achieved for a given material in a simple 2-particle sintering case in 2D.

4.6. Computing particle velocities

For postprocessing, it is convenient to output the advective velocities of individual particles during numerical simulations. In the case of the original Wang model, this information is available via the grain tracker in our code `hpsint` as $\boldsymbol{v}_{t\,i}$. However, for the coupled model, the grain tracker provides only the forces $\boldsymbol{F}_i$ acting on individual particles, and the corresponding advective velocities are computed from the displacement field using (24). To do this, we simply evaluate the displacement field $\boldsymbol{u}$ at the particle centers, which are identified during the grain tracking phase.

5. Numerical examples

5.1. Chain of identical particles in 2D

First, we apply the derived coupled approach to the chain example analyzed previously in Section 3, with the initial configuration depicted in Fig. 3(a). The material properties remain consistent with those outlined in Section 3, except for the sintering force coefficient k, which must be defined several orders of magnitude lower. This adjustment is necessary to achieve the same level of shrinkage delivered by both the generic and coupled Wang approaches for the 2-particle case, as discussed in Section 4.5.

Fig. 10(a) presents the evolution of shrinkage along the x-axis for different numbers of particles N. The results are qualitatively different from those in Fig. 4: the strain increases with the number of particles N, ultimately approaching the limiting value as anticipated by (14). The behavior pattern is no longer dependent on the magnitudes of k and M_{gb}, and all the obtained curves qualitatively show no differences. For this reason, we demonstrate here only the results for $k = 0.1$ and $M_{\mathrm{gb}} = 0.4$, presenting a more detailed complete analysis in Supplementary Material S3.2. When making this plot, we also analyzed a chain with 24 particles to demonstrate more explicitly that the obtained shrinkage evolutions indeed perfectly approach the limit curve built from (14).

In contrast to the original Wang model, the obtained strain field is strictly homogeneous, as demonstrated in Fig. 10(b), which depicts the evolution of quantity $\widetilde{\varepsilon}$ computed for individual pairs of particles in the chain with $N = 12$. Observe from expression (17) that since quantity $\widetilde{\varepsilon}$ does not account for the outer regions of the two outmost particles of the chain, it is expected for $\widetilde{\varepsilon}$ to be in agreement with the limit estimate (14) too for all values of N, as revealed in Fig. 10(b). As another consequence of having homogeneous strain field across the whole chain, the mass flow does not differ for individual necks any longer leading to identical necks, see Fig. 7(b), where the corresponding three particle pairs are indistinguishable and simply collide to a single blue line.

To plot the limit dashed curve in Fig. 10(a), the actual value of h is required for (14). Since this quantity is not directly provided by the numerical simulations, it is evaluated from the observed shrinkage ε by inverting equation (13) for $N = 10$. Note that the choice of N for this reference calculations is arbitrary, and the obtained value of h is practically identical for all the considered number of particles in the chain, as expected thanks to the consistent shrinkage behavior of the proposed coupled model.

5.2. Square domain of particles in 2D

We analyze a square 2D domain containing 40 particles having radii in the range $7.5 \ldots 13.5$, the initial configuration is shown in Fig. 11. The material properties are identical to those used in Sections 3 and

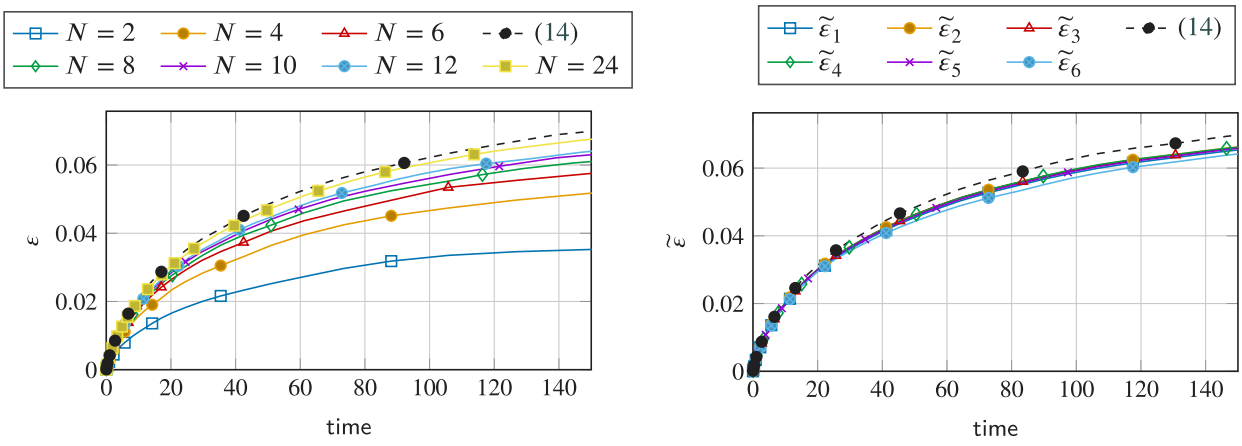

(a) Shrinkage of the particle chain with different numbers of particles N.

(b) Shrinkage strain $\widetilde{\varepsilon}_i$ computed for 6 pairs of symmetrically located particles of the chain with $N = 12$.

Fig. 10. Shrinkage behavior of the particle chain obtained with the aid of the coupled model for the sintering force coefficient $k = 0.1$ and the grain boundary diffusion prefactor $M_{gb} = 0.4$.

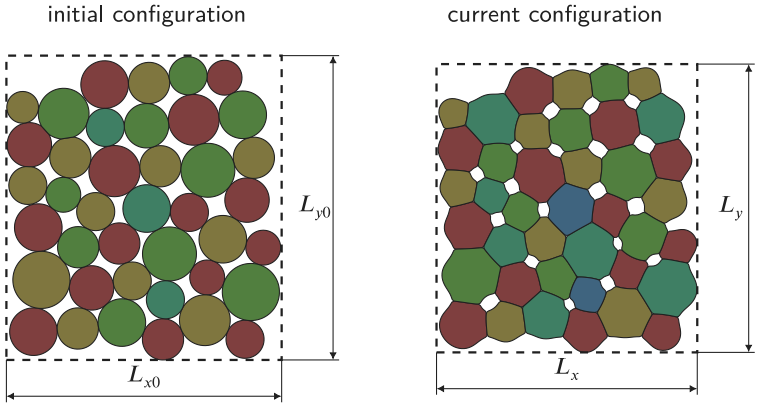

Fig. 11. The initial and current configurations of a square domain of 40 particles in 2D. The particles mapped to the same order parameter share the same color. The number of order parameters is $n_{op} = 4$ for the initial configuration and $n_{op} = 5$ for the exposed current one. Shrinkage is quantified by measuring the change in the dimensions of the packing's bounding box.

5.1. We examine four different cases: one with advection disabled and three using the coupled model with $k = 0.05$, $k = 0.1$ and $k = 0.2$. The simulation time is extended to $t_{end} = 500$ to observe the long-term effects of various shrinkage magnitudes on grain growth occurring during the later stage of sintering.

Figs. 12a–12c show shrinkage of the packing over time along the two Cartesian axes and the resultant volumetric shrinkage, respectively. These quantities are given by

$$\varepsilon_x = \frac{L_{x0} - L_x}{L_{x0}}, \tag{30a}$$

$$\varepsilon_y = \frac{L_{y0} - L_y}{L_{y0}}, \tag{30b}$$

$$\varepsilon_V = \frac{V_0 - V}{V_0} = \frac{L_{x0}L_{y0} - L_xL_y}{L_{x0}L_{y0}} \tag{30c}$$

and evaluated by constructing a bounding box around the packing at each timestep, measuring its dimensions L_x, L_y and then calculating the volume $V = L_xL_y$, as shown in Fig. 11. As seen from the plots, the advection mechanism plays a crucial role in the densification process. Interestingly, while different values of the sintering force prefactor k result in different shrinkage rates, all three cases eventually reach the same final shrinkage value. This is reasonable, since once the equilibrium concentration is achieved at the grain boundaries, no advection force is generated, and the value of k merely influences the timing of this saturation. As a result, grain growth starts earlier for larger $k = 0.2$ and later — for smaller $k = 0.05$, as observed in Fig. 12f, which shows the evolution of the average particle radius. However, Fig. 13 illustrates, the resulting microstructures for all three cases are quite similar throughout all stages of sintering — whether in the early stage ($t = 50$), the onset of the later stage ($t = 200$), or the later stage itself ($t = 500$).

The last column of Fig. 13 highlights the importance of rigid-body motions not only for shrinkage but also for the elimination of microstructural porosity. Note that this effect is more pronounced for the presented 2D case than if a 3D analysis for the same domain is performed, as seen in Supplementary Material S4. This is due to topological differences between 2D and 3D geometries and availability of additional diffusion paths from internal porosity to external surfaces in the three-dimensional case. This nuance was also revealed in [37] when comparing the pore behavior for an 8-particle 3D domain with a 4-particle 2D packing: the pore of interest gets eliminated in the former case much earlier than in the latter.

To validate the physical admissibility of the obtained results, we also examined the total free energy (2) and the total solid volume of the system, which is given by

$$\xi = \int_\Omega c \mathrm{d}\Omega. \tag{31}$$

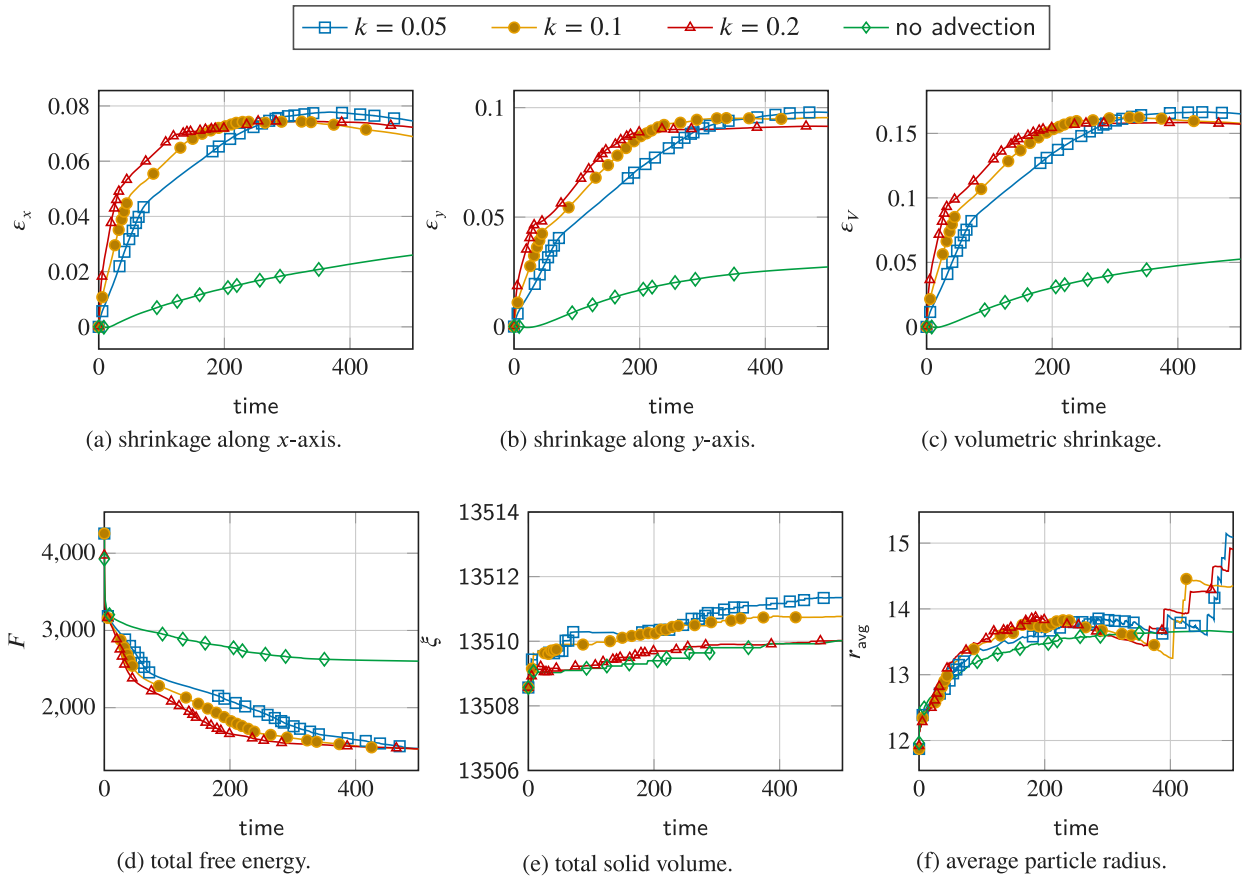

(a) shrinkage along x-axis. (b) shrinkage along y-axis. (c) volumetric shrinkage.

(d) total free energy. (e) total solid volume. (f) average particle radius.

Fig. 12. Solution metrics of a square domain of 40 particles in 2D for different sintering force coefficients k.

As expected, the former decreases and the latter remains conserved during the numerical simulations, see Figs. 12d and 12e, respectively.

5.3. Cubic domains of particles in 3D

We now switch our focus to the three-dimensional mid-scale packings shown in Fig. 14, which were also used for performance analysis in [38]. Bounding boxes of different sizes are employed to extract smaller packings containing $51 \dots 603$ particles from the largest one, which has 10245 grains. The latter was obtained through preliminary DEM simulations performed in the package `Yade` [50], following the procedure proposed in [51], which was designed to deliver an isotropic initial configuration with irregular, realistic distributions of particles having relatively low porosity. Note that, distinct from [38], the packings containing more than 1000 particles are not currently used; their investigation is deferred to future work.

The values of the energy parameters of all the simulations within this section are defined as $A = 4.35$, $B = 0.15$, $\kappa_c = 9.0$, and $\kappa_\eta = 1.79$, which render the diffuse interface thickness $w = 4$ for surface and grain boundary free energy values $\gamma_s = 1.8$ and $\gamma_{gb} = 0.6$, respectively. The sintering force coefficient is set to $k = 0.1$. The diffusion mobilities are defined as $M_{\mathrm{vo}} = 10^{-2}$, $M_{\mathrm{va}} = 10^{-3}$, $M_{\mathrm{s}} = 10.0$, $M_{\mathrm{gb}} = 4.0$, and the grain boundary mobility is set to $L = 0.1$ to suppress grain growth effects and eliminate their potential influence on the densification behavior. The initial number of divisions per interface thickness is chosen as $\zeta = 2.5$. For time marching, the BDF2 scheme is used with the initial timestep size $\tau = 0.1$, and its growth limited by the maximum value $\tau_{\max} = 100$.

Like in the previous 2D case, we study shrinkage behavior of the packings from Fig. 14. However, for the 3D case, the assessment made using (30) is less reliable than it was for the 2D analysis, since even a single particle can significantly increase the size of the bounding box in any of the three directions, thus leading to a substantially larger error in computing the packing dimensions. For this reason, in the present case, we instead evaluate the relative density using a numerical integration procedure similar to that introduced in [37] and successfully reused in [33,35]. At each timestep, the grain tracker, among other quantities, outputs particle barycenters and volumes computed using (7). We build a packing of spheres whose centers correspond to the original centroids of the grains, with radii defined such that the spheres have the same volumes as the grains. A convex hull H is then constructed around the sphere centers as illustrated for simplicity in Fig. 15 for the previously analyzed 2D case of the 40-particle square domain. Distinctly from [33,37], we do not apply the Monte–Carlo approach but instead use a simpler full sampling scheme. The bounding box of the hull is divided into a grid of uniformly distributed points with a predefined interval. Points outside the hull are discarded, and among the remaining ones, those covered by at least one sphere are counted. The ratio of the number of points lying within any of the spheres to the total number of points inside the hull then estimates the relative density of the packing $\rho_{\mathrm{rel\,Hull}}$.

Fig. 16(a) shows that all the packings exhibit very similar densification behavior, and the obtained relative density is invariant to the number of particles in the packing. This confirms admissibility of the proposed mechanism for capturing particle advection during sintering. Note that the maximum value of 0.9 is consistently observed in all simulation cases. The fact that the value of 1.0 is not reached is related to the chosen method for evaluating the packing's relative density. Although the proposed strategy, based on constructing a convex hull around the particle centers, may exclude some parts of the particles from consideration, it can also capture substantially larger void regions, leading to an overestimation of the convex hull volume and, consequently, the theoretical maximum density of the packing. As already

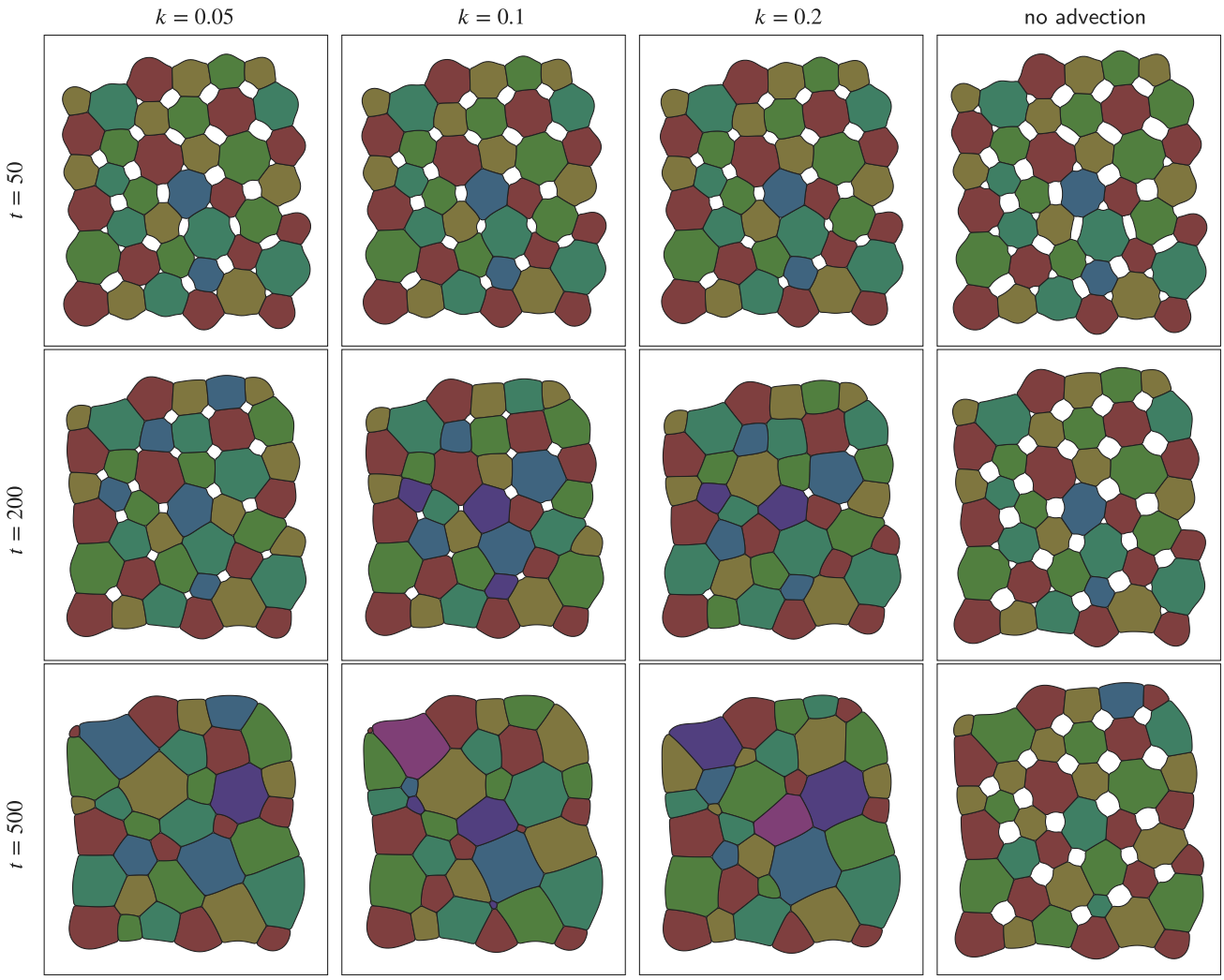

Fig. 13. Microstructures obtained for the square domain containing 40 particles in 2D for different values of the sintering force coefficient k. Particles mapped to the same order parameter share the same color. Notice, how particles are automatically remapped during simulation by the grain tracking algorithm of `hpsint`.

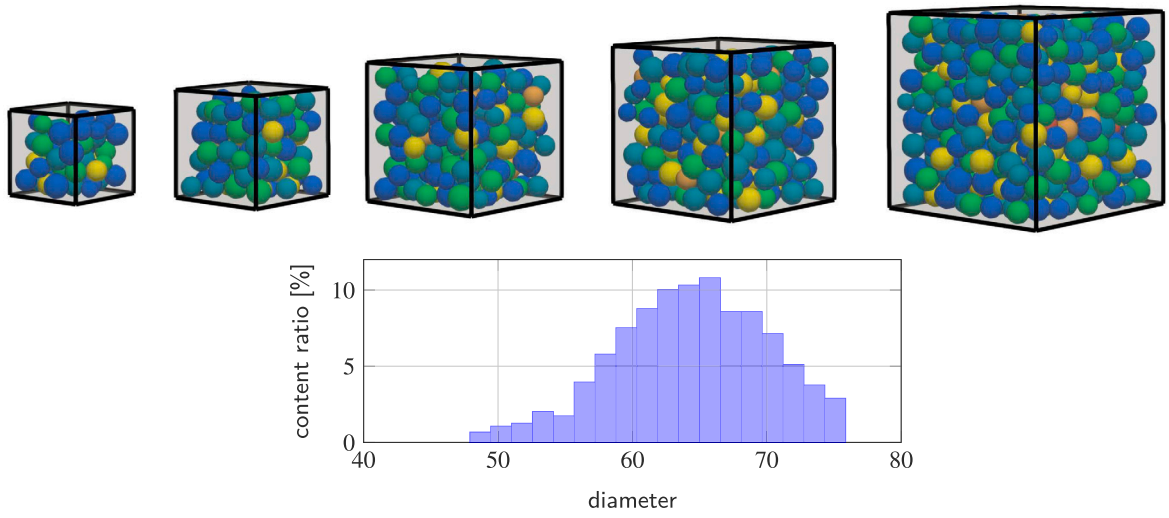

Fig. 14. Considered cubic domains of particles in 3D: 51, 102, 212, 316, and 603 particles, and the distribution of particle radii for the domain containing 603 particles.

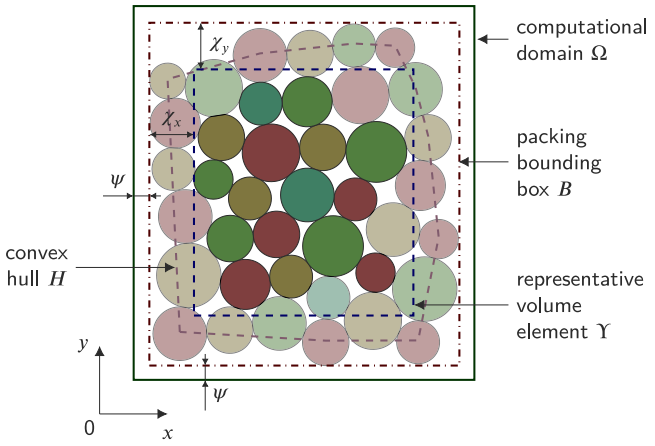

Fig. 15. The computational domain, packing bonding box, convex hull and an exemplary representative volume element (RVE) for the initial configuration of the square domain containing 40 particles in 2D. Semi-transparent particles represent those not fully captured by the RVE and are thus excluded from the evaluation of the average coordination number within the RVE.

observed in [33], for more accurate estimates of relative density, an advanced approach based on constructing concave hulls should instead be adopted.

To check whether the theoretical density value of 1.0 is achieved in the packing interior, we construct a representative volume element (RVE) within the packing, offset slightly from the boundaries of the computational domain. The relative density of this RVE is then evaluated as

$$\rho_{\text{rel RVE}} = \frac{\xi_{\text{RVE}}}{V_{\text{RVE}}}, \tag{32}$$

where ξ_{RVE} is the total solid volume in the RVE, computed by (31), and V_{RVE} is the volume of the RVE itself. Again, for simplicity, the process of building such an RVE is illustrated for the two-dimensional 40-particle square domain. As shown in Fig. 15, we use the bounding box B constructed over all particles of the packing in its initial configuration and apply a predefined padding[3] to get the desirable RVE Y. The padding is defined as follows:

$$\chi_\alpha = 0.5 r_{\max} + \vartheta L_\alpha, \tag{33}$$

where $0.5 r_{\max}$ is the radius of the largest particle in the packing and ϑL_α is the additional padding along the corresponding α-axis, where the index $\alpha = \{x, y, z\}$. Additional paddings ϑL_α are introduced to account for packing shrinkage and to ensure that none of the outer void regions enter the RVE throughout the entire simulation time range. In the present case, we anticipate approximately 10% shrinkage along each axis, as identified in the preliminary runs for the smallest packing containing 51 particles. Therefore, we choose $\vartheta = 0.1$, effectively reducing the RVE size by a value twice as large as the expected 10% shrinkage.

Fig. 16(b) shows the evolution of $\rho_{\text{rel RVE}}$ for the considered packings. Similar to Fig. 16(a), the curves are in perfect agreement with each other, thus confirming the physical plausibility of the introduced coupled densification mechanism. Notably, the maximum value of 1.0 is now achieved, indicating that no pores are left in the RVE by the end of sintering.

[3] Note that the same bounding box B is used to build a computational domain itself [38], as illustrated in Fig. 15, where the corresponding boundary padding $\psi = 0.25 r_{\max}$ is shown. In [38], we employed $\psi = 0.5 r_{\max}$, however, considering that particle systems densify during numerical simulations when using the coupled model, we have reduced the padding to $\psi = 0.25 r_{\max}$ to minimize boundary void regions in the later stages of sintering.

To further analyze the obtained microstructures, we examine the evolution of the packing coordination number N_C during densification. As mentioned in [35], the classical Coble's model [52] assumes that grains attain the shape of a tetrakaidecahedron, implying that the average coordination number in the packing, $N_{C\,\text{avg}}$, should approach the value of 14. German [53], based on literature data, derived a quadratic dependency between the relative density ρ_{rel} and the coordination number:

$$N_{C\,\text{avg}} = 2 + 11 \rho_{\text{rel}}^2 \tag{34}$$

that renders $N_{C\,\text{avg}} = 13$ for $\rho_{\text{rel}} = 1$.

To evaluate $N_{C\,\text{avg}}$, we could have employed the simplified representation of particles shown in Fig. 1, as was done for computing the relative density $\rho_{\text{rel Hull}}$. However, we opted instead to utilize the information provided by the grain tracker feature of `hpsint` [38], which enables us to compute $N_{C\,\text{avg}}$ exactly. To accomplish this, we iterate over all cells in the domain and query the grain tracker to identify which particles are located in the current cell across all order parameters. We then build the connectivity relationships between those particles. This loop computes the coordination numbers $N_{C\,i}$ for individual particles, from which the average value is directly obtained.

Fig. 16(c) illustrates the evolution of the average coordination number $N_{C\,\text{avg}}$ with respect to the relative density $\rho_{\text{rel Hull}}$. As shown, for low relative densities, $N_{C\,\text{avg}}$ remains nearly constant; however, it then begins to increase linearly, albeit with some fluctuations. The growth trend is consistent across packings with different particle counts, and as N increases, the curve approaches the reference values from the German's estimate. However, the maximum value of $\rho_{\text{rel Hull}}$ reached in Figs. 16(a) and 16(c) is 0.9 only but not 1.0. It seems that the layer of the boundary particles introduces tangible postprocessing errors, particularly in smaller packings with fewer particles.

When we filter these boundary particles out by using the RVE introduced earlier for the relative density analysis — counting only the neighbors of particles fully located inside the control volume — we obtain much better results, as seen in Fig. 16(d). The curves align closely with each other, indicating the invariance of the densification behavior with respect to the number of particles in the packing. They also agree with the assessment provided by (34). Notably, the curve for the 51-particle case primarily fluctuates between integer values, reflecting the fact that only a single grain is captured by the RVE. Clearly, having just one grain in a control volume is insufficient for a statistically meaningful analysis; however, this simple and computationally inexpensive edge case provides a qualitative understanding of the behavior of an entire family of packings with similar particle size distributions. Interestingly, as depicted in Fig. 17, the number of order parameters n_{op} in use, which is dynamically adjusted during the simulation, correlates well with the average coordination number of the packing, allowing thus the grain tracker technical information to be leveraged for estimating $N_{C\,\text{avg}}$.

To understand how the reported metrics correlate with the obtained microstructures, selected configurations of the 603-particle packing are presented in Fig. 18. It is evident that there is an overall volumetric shrinkage of the packing and a polyhedralization of the grains during sintering.

6. Conclusion

This work has proposed a novel solid-state sintering model that directly couples the well-known phase-field model of thermodynamic mass transport during sintering [22] with the balance of momentum of linear elasticity. It addresses one of the main drawbacks of the model introduced by Wang [22]: the fact that the particle advection velocities are proportional to the sintering forces, leading to a rigid-body motion behavior that fails to account for the long-range interactions among particles as components of a mechanical system. In contrast, our new model defines distributed body forces equivalent to Wang's sintering

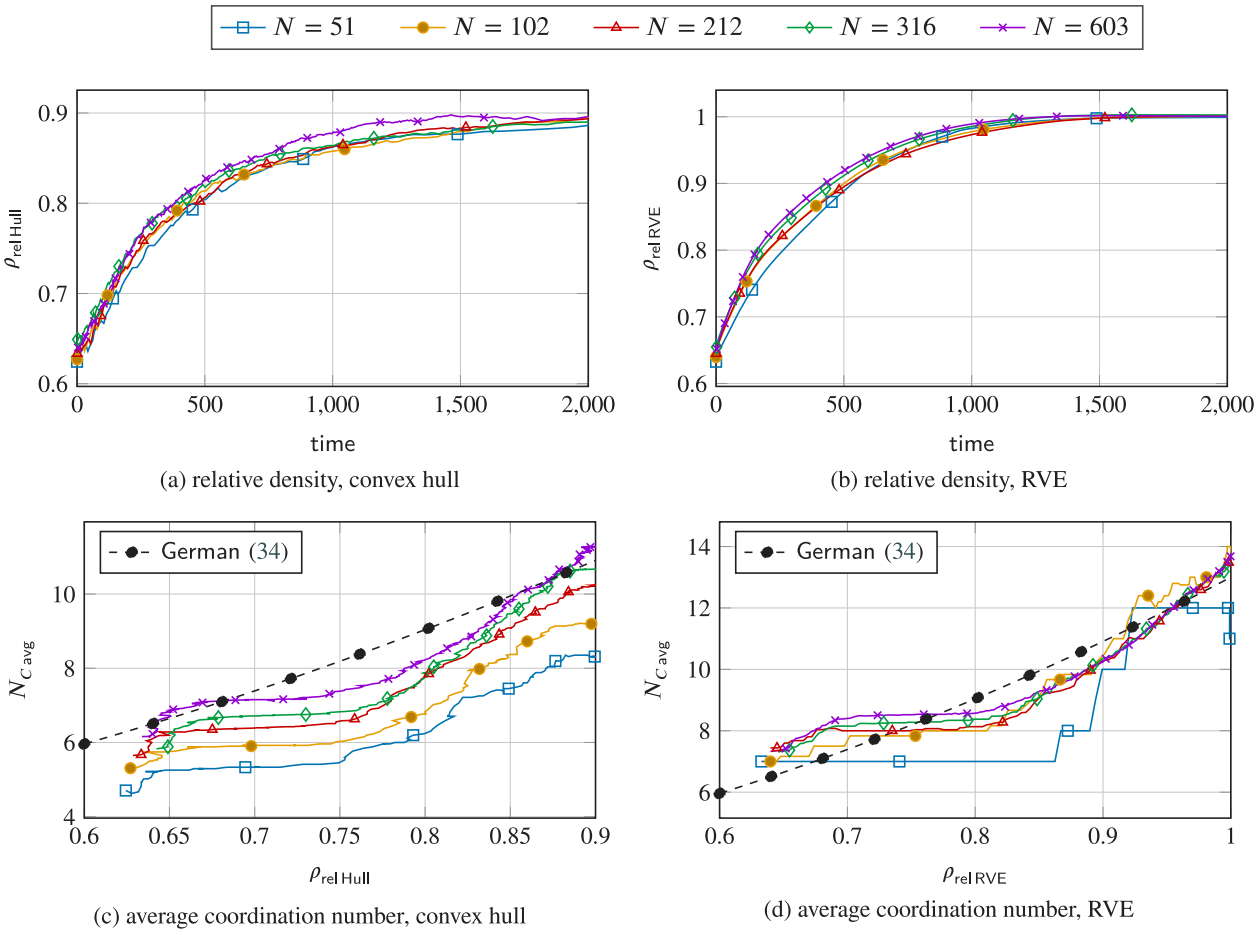

(a) relative density, convex hull

(b) relative density, RVE

(c) average coordination number, convex hull

(d) average coordination number, RVE

Fig. 16. Relative density and average coordination number evolutions for the considered cubic domains of particles in 3D estimated using (i) spatial integration of the convex hull region built around the centers of spheres representing individual particles, and (ii) a specifically constructed representative volume element.

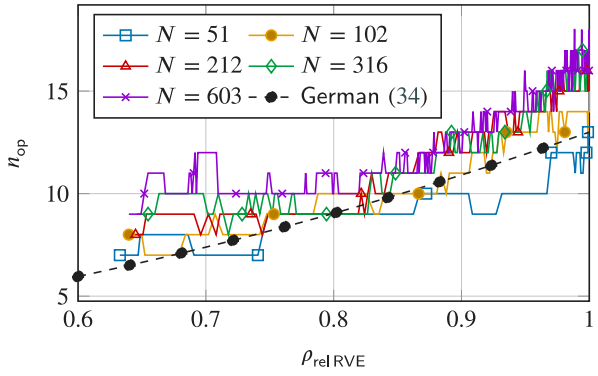

Fig. 17. Evolution of the number of order parameters during sintering simulations for the considered cubic domains of particles in 3D.

forces. It utilizes these body forces to solve a linear elasticity problem that accounts for long-range interactions between particles, thereby realistically conceptualizing them as parts of a cohesive mechanical body. Our model emphasizes the necessity of simulating sintering as a coupled (multiphysics) problem to obtain plausible, physically meaningful results.

To support this claim, we analyzed a simple particle chain benchmark problem. In this scenario, the original sintering force concept proposed by Wang [22] reveals an unphysical dependency of shrinkage on the system size, renders a nonhomogeneous strain field and unphysical oscillations in certain regions of the packing. By contrast, our new model naturally overcame all these issues through its more realistic representation of the underlying physics of sintering.

Currently, our model relies on several simplifying assumptions, such as the notion that the mechanical stress generated during the sintering process relaxes infinitely fast (or at least much faster than the diffusive mass transport). However, these are not inherent to our modeling concept; rather, they have been made for the sake of simplicity in this proof-of-concept contribution. We plan to replace them with more realistic assumptions in future work.

In addition to these major contributions, we have replaced the discontinuous grain boundary filter function originally proposed by Wang [22] with a novel continuous smooth alternative. This new formulation is more suitable for discretized numerical solution schemes and results in improved convergence of the applied iterative solvers.

The numerical implementation of our new model is based on the high-performance FEM code `hpsint` [38], which employs various holistic optimizations, including but not limited to the tailored block preconditioner, the distributed graph-based grain tracking algorithm, and fast matrix-free evaluation kernels, all aimed at providing superior efficiency in MPI environments. For the preconditioning of the coupled model, we extended the previously proposed block preconditioner by incorporating a regular AMG block that handles the linear mechanics equations.

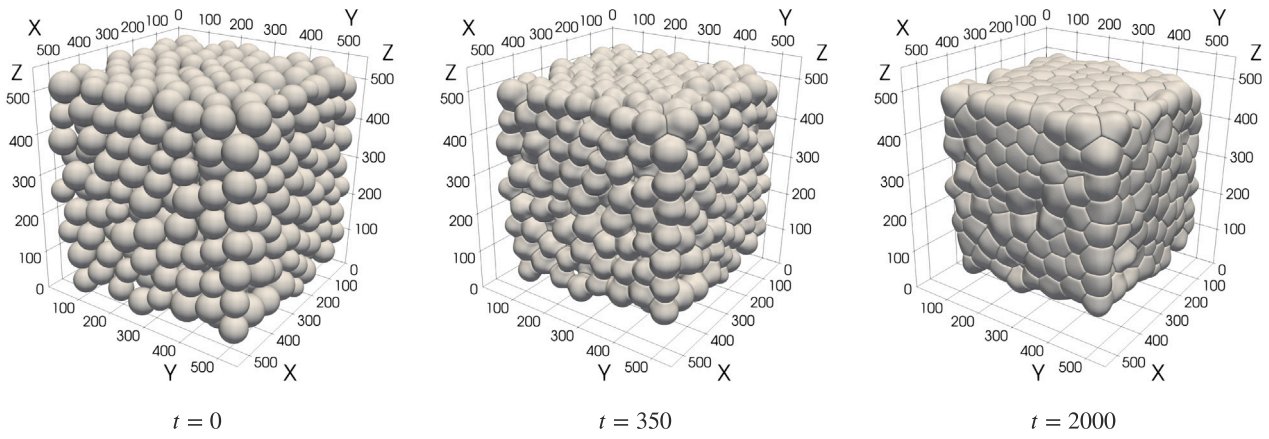

Fig. 18. Three-dimensional view of the 603-particle domain at selected time instances. The axes grid is adjusted to be identical for all three time instances such that the packing shrinkage is clearly visible.

CRediT authorship contribution statement

Vladimir Ivannikov: Writing – review & editing, Writing – original draft, Visualization, Validation, Software, Investigation, Conceptualization. **Peter Munch:** Writing – review & editing, Writing – original draft, Visualization, Validation, Software, Methodology. **Thomas Ebel:** Writing – review & editing, Supervision, Methodology, Investigation. **Regine Willumeit–Römer:** Writing – review & editing, Supervision, Investigation, Funding acquisition. **Christian J. Cyron:** Writing – review & editing, Supervision, Methodology, Funding acquisition, Formal analysis, Conceptualization.

Declaration of Generative AI and AI-assisted technologies in the writing process

During the preparation of this work the authors used ChatGPT 4o in order to improve the readability and language of the manuscript. After using this tool, the authors reviewed and edited the content as needed and take full responsibility for the content of the published article.

Declaration of competing interest

The authors declare that they have no known competing financial interests or personal relationships that could have appeared to influence the work reported in this paper.

Acknowledgment

The authors acknowledge collaboration with Martin Kronbichler as well as the `deal.II` community. The authors gratefully acknowledge the Gauss Centre for Supercomputing e.V. (www.gauss-centre.eu) for supporting this project by providing computing time on the GCS Supercomputer SuperMUC-NG at Leibniz Supercomputing Centre (LRZ, www.lrz.de) through project id pn36li.

Appendix A. Supplementary data

Supplementary material related to this article can be found online at https://doi.org/10.1016/j.commatsci.2025.113844.

Data and code availability

The model was implemented in the open-source framework `hpsint` available on GitHub (https://github.com/hpsint/hpsint). The raw data required to reproduce the presented findings can be provided by the authors upon a reasonable request.

References

[1] Thomas Ebel, Vera Friederici, Philipp Imgrund, Thomas Hartwig, 19 - Metal injection molding of titanium, in: Ma Qian, Francis H. (Sam) Froes (Eds.), Titanium Powder Metallurgy, Butterworth-Heinemann, Boston, 2015, pp. 337–360.

[2] Marius A. Wagner, Amir Hadian, Tutu Sebastian, Frank Clemens, Thomas Schweizer, Mikel Rodriguez-Arbaizar, Efrain Carreño-Morelli, Ralph Spolenak, Fused filament fabrication of stainless steel structures - from binder development to sintered properties, Addit. Manuf. 49 (2022) 102472.

[3] Christopher Gloeckle, Thomas Konkol, Olaf Jacobs, Wolfgang Limberg, Thomas Ebel, Ulrich A. Handge, Processing of highly filled polymer-metal feedstocks for fused filament fabrication and the production of metallic implants, Materials 13 (19) (2020).

[4] Eshwara Phani Shubhakar Nidadavolu, Diana Krüger, Berit Zeller-Plumhoff, Domonkos Tolnai, Björn Wiese, Frank Feyerabend, Thomas Ebel, Regine Willumeit-Römer, Pore characterization of PM Mg–0.6Ca alloy and its degradation behavior under physiological conditions, J. Magnes. Alloy. 9 (2) (2021) 686–703.

[5] Shotaro Hara, Akihiro Ohi, Naoki Shikazono, Sintering analysis of sub-micron-sized nickel powders: Kinetic Monte Carlo simulation verified by FIB–SEM reconstruction, J. Power Sources 276 (2015) 105–112.

[6] Michael Braginsky, Veena Tikare, Eugene Olevsky, Numerical simulation of solid state sintering, Int. J. Solids Struct. 42 (2) (2005) 621–636, Micromechanics of Materials.

[7] Veena Tikare, Michael Braginsky, Didier Bouvard, Alexander Vagnon, Numerical simulation of microstructural evolution during sintering at the mesoscale in a 3D powder compact, Comput. Mater. Sci. 48 (2) (2010) 317–325.

[8] Rasmus Bjørk, Henrik Lund Frandsen, Veena Tikare, Eugene Olevsky, Nini H. Pryds, Strain in the mesoscale kinetic Monte Carlo model for sintering, Comput. Mater. Sci. 82 (2014) 293–297.

[9] Christophe L. Martin, L.C.R. Schneider, L. Rafael Olmos, Didier Bouvard, Discrete element modeling of metallic powder sintering, Scr. Mater. 55 (5) (2006) 425–428.

[10] Sylvain Martin, Sebastián Navarro, Hervé Palancher, Anne Bonnin, Jacques Léchelle, Mohamed Guessasma, Jérôme Fortin, Khashayar Saleh, Validation of DEM modeling of sintering using an in situ X-ray microtomography analysis of the sintering of NaCl powder, Comput. Part. Mech. 3 (4) (2016) 525–532.

[11] Szymon Nosewicz, Jerzy Rojek, Marcin Chmielewski, Discrete element framework for determination of sintering and postsintering residual stresses of particle reinforced composites, Materials 13 (18) (2020).

[12] Brayan Paredes-Goyes, David Jauffres, Jean-Michel Missiaen, Christophe L. Martin, Grain growth in sintering: A discrete element model on large packings, Acta Mater. 218 (2021) 117182.

[13] Johannes Hötzer, Andreas Reiter, Henrik Hierl, Philipp Steinmetz, Michael Selzer, Britta Nestler, The parallel multi-physics phase-field framework Pace3D, J. Comput. Sci. 26 (2018) 1–12.

[14] Johannes Hötzer, Marco Seiz, Michael Kellner, Wolfgang Rheinheimer, Britta Nestler, Phase–field simulation of solid state sintering, Acta Mater. 164 (2019) 184–195.

[15] Supriyo Ghosh, Christopher K. Newman, Marianne M. Francois, Tusas: A fully implicit parallel approach for coupled phase-field equations, J. Comput. Phys. 448 (2022) 110734.

[16] OpenPhase, OpenPhase software library for phase-field simulations, 2023.

[17] Raphael Schiedung, Reza Darvishi Kamachali, Ingo Steinbach, Fathollah Varnik, Multi-phase-field model for surface and phase-boundary diffusion, Phys. Rev. E 96 (2017) 012801.

[18] Stephen DeWitt, Shiva Rudraraju, David Montiel, W Beck Andrews, Katsuyo Thornton, PRISMS-PF: A general framework for phase-field modeling with a matrix-free finite element method, Npj Comput. Mater. 6 (1) (2020) 1–12.
[19] Derek Gaston, Chris Newman, Glen Hansen, Damien Lebrun-Grandié, MOOSE: A parallel computational framework for coupled systems of nonlinear equations, Nucl. Eng. Des. 239 (10) (2009) 1768–1778.
[20] Karthikeyan Chockalingam, Varvara G. Kouznetsova, Olaf van der Sluis, Marc G.D. Geers, 2D phase field modeling of sintering of silver nanoparticles, Comput. Methods Appl. Mech. Engrg. 312 (2016) 492–508.
[21] Sudipta Biswas, Daniel Schwen, Vikas Tomar, Implementation of a phase field model for simulating evolution of two powder particles representing microstructural changes during sintering, J. Mater. Sci. 53 (8) (2018) 5799–5825.
[22] Yu U. Wang, Computer modeling and simulation of solid-state sintering: A phase field approach, Acta Mater. 54 (4) (2006) 953–961.
[23] Jie Deng, A phase field model of sintering with direction-dependent diffusion, Mater. Trans. 53 (2) (2012) 385–389.
[24] Karim Ahmed, Clarissa A. Yablinsky, A. Schulte, Todd Allen, Anter El-Azab, Phase field modeling of the effect of porosity on grain growth kinetics in polycrystalline ceramics, Modelling Simul. Mater. Sci. Eng. 21 (6) (2013) 065005.
[25] Sudipta Biswas, Daniel Schwen, Hao Wang, Maria Okuniewski, Vikas Tomar, Phase field modeling of sintering: Role of grain orientation and anisotropic properties, Comput. Mater. Sci. 148 (2018) 307–319.
[26] Cody J. Permann, Michael R. Tonks, Bradley Fromm, Derek R. Gaston, Order parameter re-mapping algorithm for 3D phase field model of grain growth using FEM, Comput. Mater. Sci. 115 (2016) 18–25.
[27] Robert Termuhlen, Xanthippi Chatzistavrou, Jason D. Nicholas, Hui-Chia Yu, Three-dimensional phase field sintering simulations accounting for the rigid-body motion of individual grains, Comput. Mater. Sci. 186 (2021) 109963.
[28] Fadi Abdeljawad, Dan S. Bolintineanu, Adam Cook, Harlan Brown-Shaklee, Christopher DiAntonio, Daniel Kammler, Allen Roach, Sintering processes in direct ink write additive manufacturing: A mesoscopic modeling approach, Acta Mater. 169 (2019) 60–75.
[29] Rongpei Shi, Marissa Wood, Tae Wook Heo, Brandon C. Wood, Jianchao Ye, Towards understanding particle rigid-body motion during solid-state sintering, J. Eur. Ceram. Soc. 41 (16) (2021) 211–231.
[30] Branislav Dzepina, Daniel Balint, Daniele Dini, A phase field model of pressure-assisted sintering, J. Eur. Ceram. Soc. 39 (2) (2019) 173–182.
[31] Vladimir Ivannikov, Fritz Thomsen, Thomas Ebel, Regine Willumeit-Römer, Capturing shrinkage and neck growth with phase field simulations of the solid state sintering, Modelling Simul. Mater. Sci. Eng. 29 (7) (2021) 075008.
[32] Marco Seiz, Effect of rigid body motion in phase-field models of solid-state sintering, Comput. Mater. Sci. 215 (2022) 111756.
[33] Marco Seiz, Henrik Hierl, Britta Nestler, An improved grand-potential phase-field model of solid-state sintering for many particles, Modelling Simul. Mater. Sci. Eng. 31 (5) (2023) 055006.
[34] Hans Lukas, Suzana G. Fries, Bo Sundman, Computational Thermodynamics: The Calphad Method, Cambridge University Press, Cambridge, 2007.
[35] Marco Seiz, Henrik Hierl, Britta Nestler, Unravelling densification during sintering by multiscale modelling of grain motion, J. Mater. Sci. 58 (35) (2023) 14051–14071.
[36] Kazunari Shinagawa, Simulation of grain growth and sintering process by combined phase-field/discrete-element method, Acta Mater. 66 (2014) 360–369.
[37] Ian Greenquist, Michael R. Tonks, Larry K. Aagesen, Yongfeng Zhang, Development of a microstructural grand potential-based sintering model, Comput. Mater. Sci. 172 (2020) 109288.
[38] Peter Munch, Vladimir Ivannikov, Christian Cyron, Martin Kronbichler, On the construction of an efficient finite-element solver for phase-field simulations of many-particle solid-state-sintering processes, Comput. Mater. Sci. 231 (2024) 112589.
[39] Pasquale C. Africa, Daniel Arndt, Wolfgang Bangerth, Bruno Blais, Marc Fehling, Rene Gassmöller, Timo Heister, Luca Heltai, Sebastian Kinnewig, Martin Kronbichler, Matthias Maier, Peter Munch, Magdalena Schreter-Fleischhacker, Jan P. Thiele, Bruno Turcksin, David Wells, Vladimir Yushutin, The deal.II library, Version 9.6, J. Numer. Math. 32 (4) (2024) 369–380.
[40] Martin Kronbichler, Katharina Kormann, A generic interface for parallel cell-based finite element operator application, Comput. & Fluids 63 (2012) 135–147.
[41] Daniel Arndt, Wolfgang Bangerth, Denis Davydov, Timo Heister, Luca Heltai, Martin Kronbichler, Matthias Maier, Jean-Paul Pelteret, Bruno Turcksin, David Wells, The deal.II finite element library: Design, features, and insights, Comput. Math. Appl. 81 (2021) 407–422.
[42] Carl E. Krill III, Long-Qing Chen, Computer simulation of 3-D grain growth using a phase-field model, Acta Mater. 50 (12) (2002) 3059–3075.
[43] Srikanth Vedantam, B.S.V. Patnaik, Efficient numerical algorithm for multiphase field simulations, Phys. Rev. E 73 (2006) 016703.
[44] D. Lynn Johnson, New method of obtaining volume, grain–boundary, and surface diffusion coefficients from sintering data, J. Appl. Phys. 40 (1) (1969) 192–200.
[45] George K. Batchelor, An Introduction to Fluid Dynamics, in: Cambridge Mathematical Library, Cambridge University Press, Cambridge, 2000.
[46] Antonio Rodríguez-Ferran, Folco Casadei, Antonio Huerta, ALE stress update for transient and quasistatic processes, Internat. J. Numer. Methods Engrg. 43 (2) (1998) 241–262.
[47] Antonio Rodríguez-Ferran, Agustí Pérez-Foguet, Antonio Huerta, Arbitrary Lagrangian–Eulerian (ALE) formulation for hyperelastoplasticity, Internat. J. Numer. Methods Engrg. 53 (8) (2002) 1831–1851.
[48] Michael Heroux, Roscoe Bartlett, Vicki Howle Robert Hoekstra, Jonathan Hu, Tamara Kolda, Richard Lehoucq, Kevin Long, Roger Pawlowski, Eric Phipps, Andrew Salinger, et al., An Overview of Trilinos, Citeseer, Albuquerque, 2003.
[49] Michael W. Gee, Christopher M. Siefert, Jonathan J. Hu, Ray S. Tuminaro, Marzio G. Sala, ML 5.0 smoothed aggregation user's guide, 2006.
[50] V. Smilauer, et al., Yade Documentation 2nd ed, The Yade Project, Zenodo, 2015, http://yade-dem.org/doc/.
[51] Vladimir Ivannikov, Fritz Thomsen, Thomas Ebel, Regine Willumeit-Römer, Coupling the discrete element method and solid state diffusion equations for modeling of metallic powders sintering, Comput. Part. Mech. 10 (2) (2023) 185–207.
[52] Robert L. Coble, Sintering crystalline solids. I. Intermediate and final state diffusion models, J. Appl. Phys. 32 (5) (1961) 787–792.
[53] Randall M. German, Coordination number changes during powder densification, Powder Technol. 253 (2014) 368–376.